LBNL-49247

ERNEST ORLANDO LAWRENCE
BERKELEY NATIONAL LABORATORY

Formation and Transport in Hubbard Bands in Ge:Cu

Hughes H. Silvestri

Materials Sciences Division
Center for Advanced Materials

December 2001

M.S. Thesis

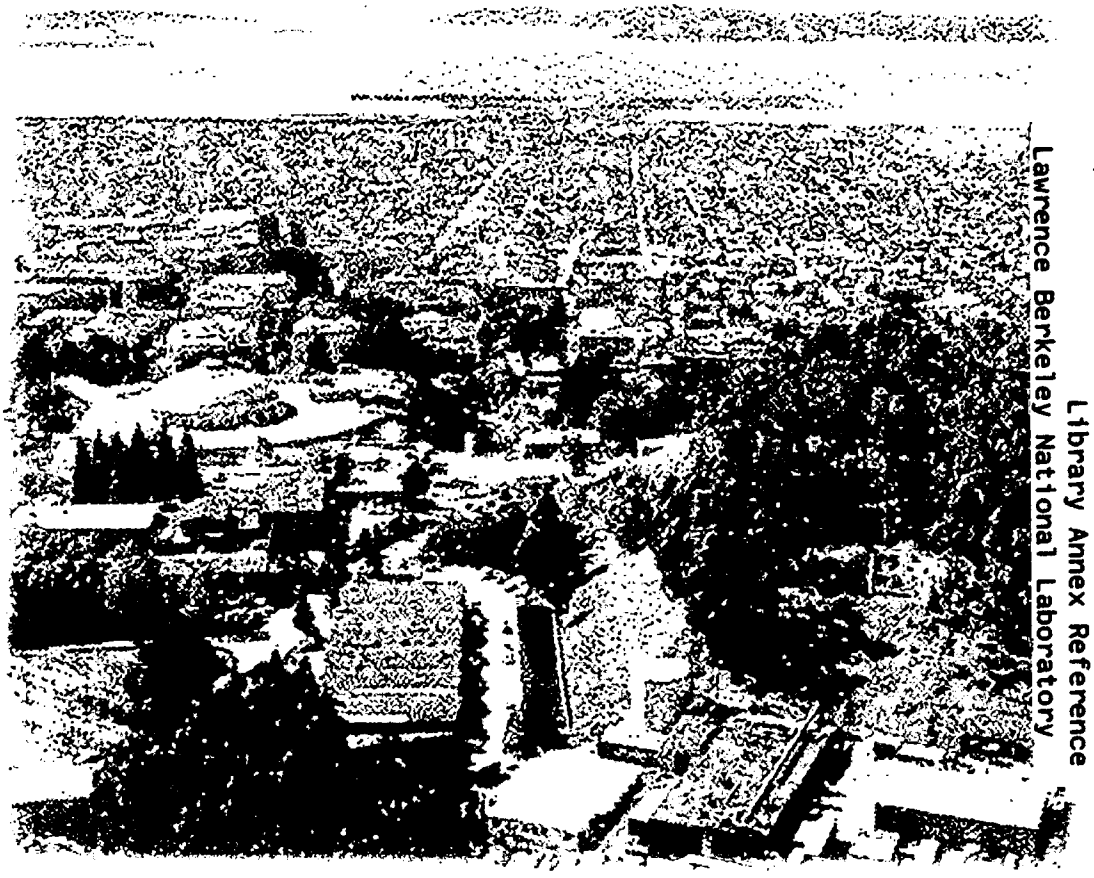

DISCLAIMER

LBNL-49247

Formation and Transport in Hubbard Bands in Ge:Cu

Hughes Howland Silvestri

Materials Science and Engineering
University of California, Berkeley

and

Center for Advanced Materials
Materials Sciences Division
Ernest Orlando Lawrence Berkeley National Laboratory
1 Cyclotron Road
Berkeley, California 94720

M.S. Thesis

December 2001

This work was supported by the Director, Office of Science, Office of Basic Energy Sciences, Materials Sciences Division, of the U.S. Department of Energy under Contract No. DE-AC03-76SF00098.

Formation and Transport in Hubbard bands in Ge:Cu

by

Hughes Howland Silvestri

B.S. (Fairfield University) 1997

A thesis submitted in partial satisfaction of the

requirements for the degree of

Master of Science

in

Engineering – Materials Science and Engineering

in the

GRADUATE DIVISION

of the

UNIVERSITY OF CALIFORNIA, BERKELEY

Committee in charge:

Prof. Eugene E. Haller, Chair
Prof. Oscar D. Dubon
Prof. Alan M. Portis

Fall 2001

Acknowledgments

I would like to thank Professor Eugene Haller for his continuous support and guidance both on this project and throughout my graduate career. I would also like to thank Professors Alan Portis and Oscar Dubon for their efforts in reviewing my thesis.

I am grateful for the help and support of the members of the Haller group. I would specifically like to thank the staff scientists; Jeff Beeman for all of his hard work in helping me with the low temperature measurements and Dr. Wladek Walukiewicz for his work in analyzing and helping me to understand the complex theories involved in this research. I would also like to thank David Hom for his continued assistance at LBNL.

I would like to acknowledge the aid of former members of the Haller group, Chris, Danielle, Marlene, Dawnelle, and Raechelle, whose advice and friendship has been essential to my success. I would also like to thank Oscar who began this research as a graduate student and has continued to make tremendous contributions to the work. His guidance and advice has been invaluable.

I would like to thank my family for their constant support and encouragement, as well as their sacrifice and effort that has allowed me to pursue my goals. I would like to thank my friends for their support, and to Roman for keeping me focused and pushing me to achieve. I would like to thank Prof. Nancy Haegel for believing in me.

This work was supported by the Director, Office of Science, Office of Basic Energy Sciences, Division of Materials Sciences, U.S. Department of Energy under Contract No. DE-AC03-76SF00098.

Table of Contents

1 Introduction

The electronic properties of different materials vary greatly. Based on these properties, materials are sorted into three categories: metal, insulator, or semiconductor. At the extremes of electrical conduction are metals, which display little resistance to the flow of electrical current, and insulators, which exhibit extremely low electrical conductivity. Semiconductors, as the name would suggest, have properties in between that of metals and insulators; that is, they show modest electrical conduction that can be increased dramatically with the addition of energy to the material. The focus of this work will be to study how semiconductors undergo the change from a quasi "insulating" state to a "metallic" state, or as it is called, a Metal-Insulator Transition (MIT).

The electronic properties of semiconductors arise primarily from impurities and defects present in the material. Elemental impurities can sit substitutionally within the crystalline lattice of a semiconductor and may have a different number of valence shell electrons than the host lattice. If the impurity has more electrons than required to form a Lewis octet, it adds an electron to the semiconductor creating what is known as a donor. An impurity species with fewer valence electrons than the host elements will take or "accept" an electron to complete its Lewis octet, creating a "hole" or the absence of one electron in the lattice. Impurities of this type are known as acceptors. The ability to accept or donate electrons is associated with a binding energy represented by energy levels within the forbidden energy gap of a semiconductor.

Because the type of electrical activity depends on the number of electrons in the valence shell of the impurity, in general, elements to the right or left of the host species on the periodic table form acceptors or donors, respectively. Elements in columns immediately to the right or left will bind or donate one electron, making them single

acceptors or donors. If the element has a valence shell difference of two or even three electrons it may exist within the host lattice as a double or triple acceptor or donor.

The energy with which an impurity binds an electron or hole and the resulting energy levels created can be described by the effective mass theory using the hydrogenic model. This model uses the analogy of a hydrogen atom binding a single electron to determine the binding energy and effective Bohr radius of the electron or hole bound to the impurity [1]. The formalism of the effective mass theory was developed by Kittel and Mitchell [2], and Luttinger and Kohn [3]. The present treatment is intended to introduce the concepts and equations, for a more thorough discussion, the reader is directed to the above works.

The physics of the electronic states of the hydrogen atom is well established. The case of a charge bound to an impurity within a host lattice differs from a free hydrogen atom in that the charge carrier sees a homogenous medium with an average dielectric constant ε, corresponding to the dielectric constant of the host material, rather than free space. Also, the mass of the electron or hole is different from that of the free electron. The charge carrier must exist within one of the partially filled energy bands of the material to move throughout the crystal. Therefore it is the mass of the charge carrier within the energy band that must be used in the hydrogenic model. This effective mass is dependent on the band by the following relation:

$$m_{eff} = \hbar^2 \left(\frac{\partial^2 E}{\partial |\vec{k}|^2} \right)^{-1} \tag{1.1}$$

where m_{eff} is the effective mass of the charge carrier and it is inversely proportional to the curvature of the band given by a dispersion (E-k) relationship.

Given an effective mass from Equation 1.1 and the dielectric constant of the host lattice, the equations for the binding energy and Bohr radius of the hydrogen atom are

modified to yield the corresponding properties for impurities within semiconductors, as follows:

$$E = E_H \frac{m^*}{m_e}\frac{1}{\varepsilon^2} = 13.6eV\frac{m^*}{m_e}\frac{1}{\varepsilon^2} \tag{1.2}$$

and

$$r_{Bohr} = \frac{4\pi\varepsilon_0 h^2}{m_e e^2}\frac{m_e}{m^*}\varepsilon = 0.5\mathring{A}\frac{m_e}{m^*}\varepsilon \tag{1.3}$$

The result of Equation 1.2 is that the ground state binding energy of the hydrogen atom has been modified by the ratio of the effective mass to the free carrier mass and the inverse of square of the dielectric constant. This gives a resulting binding energy for electrons and holes bound to impurities that is much smaller (on the order of meV) than that of the hydrogen atom (13.6 eV).

The effective Bohr radius for an electron or hole bound to an impurity is modified from that of the hydrogen atom by the inverse effective mass ratio and the dielectric constant, as seen in Equation 1.3. This results in a much larger effective Bohr radius for impurities (~30-150 Å) than the hydrogen atom (0.5 Å). This is not surprising when the effects of the screening by the additional charges present in the semiconductor is taken into consideration – as it is with the dielectric constant.

Shallow impurities, which are impurities with small binding energies, have their energy levels located very near to an energy band extremum. Having binding energies on the order of room temperature thermal energy (~25 meV), shallow impurities will donate their electrons or holes to the conduction or valence band adding to the conductivity of the crystal.

In lightly doped semiconductors, the only means by which charge carriers bound to impurities can conduct is via the input of energy (thermal, optical, etc.), exciting the carrier to the valence or conduction band. In heavily doped semiconductors, the carriers can travel between impurity states within the bandgap without the addition of energy. It is by this

addition of extra impurities that a semiconductor can undergo a Metal-Insulator Transition (MIT). This topic will be discussed in greater detail in Section 1.2.2.

1.1 Copper in Germanium

Germanium, an elemental group IV semiconductor, can be purified to levels unachievable in other semiconductors. Impurity concentrations down to 10^9 atoms/cm^3 have been demonstrated [4]. In spite of the tremendous efforts at removing impurities in this material, one omnipresent impurity in germanium is copper [5]. Therefore, in order to work with germanium, one must fully understand the effects that copper has in the material, and what effects processing the material will have on the Cu impurities.

Copper has been shown to have many interesting properties in germanium. It can exist as both a substitutional and interstitial impurity simultaneously in the host lattice. In its substitutional lattice position, it has been found to be a triple acceptor, meaning that it can bind up to three holes [6]. In an interstitial position, Cu exists as a positive ion, yielding a donor-like state [7]. Copper diffuses primarily by the dissociative mechanism, meaning that it travels interstitially through the lattice before coming to rest at a substitutional position by recombining with a vacancy [8]. This gives Cu a much larger diffusivity (2×10^{-7} cm^2/s at 700°C) in Ge as compared to substitutional impurity atoms [9].

The triple-acceptor nature of the Cu impurity in Ge has given rise to its primary application. Copper in Ge has a very broad absorption spectrum, making it useful for infrared photoconductors. Figure 1.1 presents an absorption spectrum of Ge:Cu, illustrating the large absorption range of the material. Copper doped germanium photoconductors are used as detectors for infrared spectroscopy techniques like Local Vibrational Mode (LVM) spectroscopy [10].

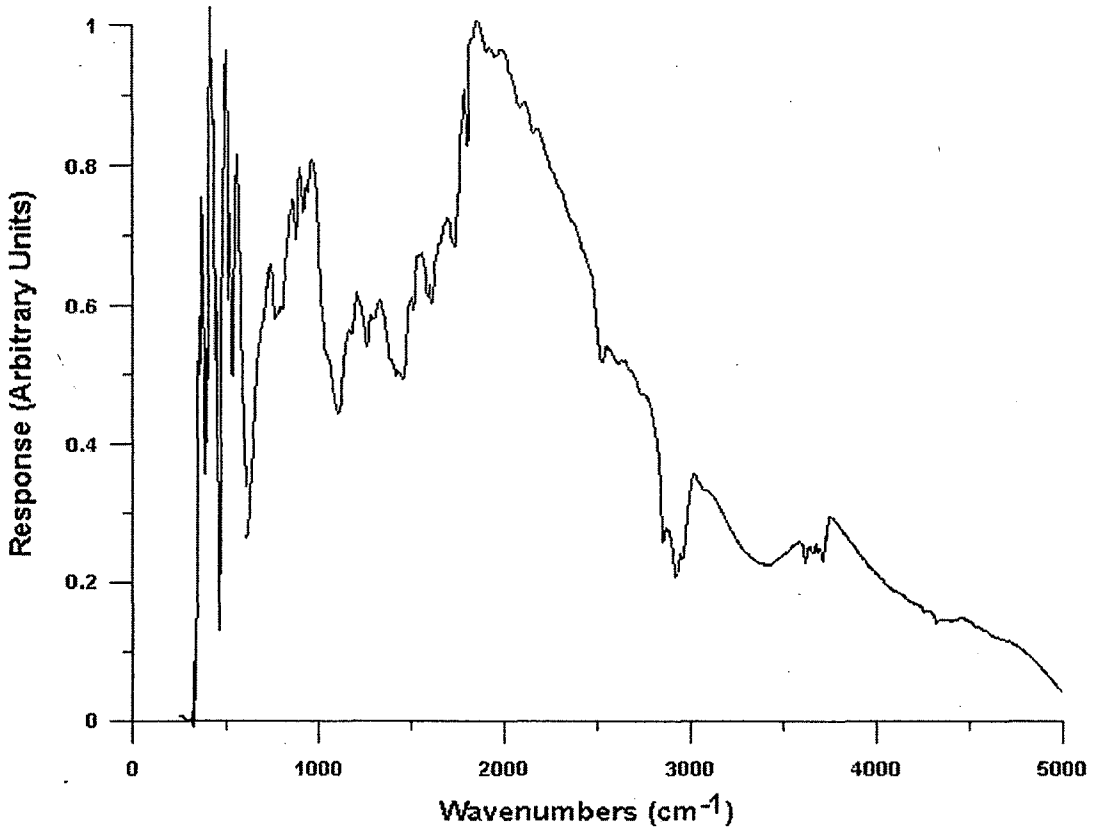

Figure 1.1 Absorption spectrum of copper doped germanium, demonstrating the broad absorption range. Uncorrected for beamsplitter absorption. (Courtesy J.W. Beeman)

1.1.1 Diffusion of Copper in Germanium

The motion of the copper through the germanium lattice can be described with the dissociative or Frank-Turnbull mechanism [8]. This mechanism describes a copper atom traveling through the lattice by changing from a substitutional position to an interstitial position by creation of a lattice vacancy and copper interstitial pair:

$$Cu_s \longleftrightarrow Cu_i + V \tag{1.4}$$

The copper then moves interstitially through the crystal until it encounters another vacancy. The vacancy and interstitial copper will recombine to form a substitutional copper atom.

This mechanism is only possible because both interstitial and substitutional species of copper exist in a germanium crystal simultaneously.

Because of this dual nature of the copper impurity in germanium, the diffusion and solubility of copper in germanium have been widely studied [9,11,12]. Studies of the precipitation behavior showed that the substitutional copper concentration could be controlled by annealing germanium at a specific elevated temperature and then rapidly quenching it [6,13,14]. By heating the germanium to high temperatures, a large equilibrium vacancy concentration is created which allows interstitial copper atoms to find substitutional positions in the lattice. When the germanium is rapidly quenched, the copper atoms are frozen into the substitutional positions in the lattice and become electrically active. Hall and Racette [11] determined the interstitial and substitutional copper concentrations as functions of quench temperature. (Also see Figure 3.1) The total Cu concentration was found by diffusing radioactive ^{64}Cu into Ge from the surface and measuring the γ activity to determine the concentration. Electrical measurements were used to determine the fraction of Cu occupying lattice sites (forming triple acceptors).

Based on the solubility data from Hall and Racette [11], as well as Woodbury and Tyler [6], copper diffusion at elevated temperatures and rapid quenching was used to create the samples of different copper concentrations for this work.

1.1.2 Electronic States of Cu in Ge

Much of the research on copper in germanium has focused, in the past, on the electronic properties of the substitutional copper impurity. The special interest in this impurity was due, in part, to its triple acceptor nature, the very high diffusivity, and the many interesting properties which were observed as a result. Woodbury and Tyler [6] used Hall effect measurements to determine the energy levels of the three acceptor states.

The shallowest level of substitutional copper ($Cu^{0/-}$) was found to be bound with an activation energy of $E_v + 43$ meV. The second level ($Cu^{-/--}$) was determined to sit near mid-gap at $E_v + 330$ meV. The third energy level of the substitutional copper state ($Cu^{--/---}$) was found to sit at $E_c - 260$ meV. The existence of the third level in the upper half of the band gap has resulted in the observation of donor- like properties of that state. Clauws, et al. [15], reported electron trapping behavior of the third acceptor level observed via Deep Level Transient Spectroscopy (DLTS). This technique uses the capacitance transients induced in a diode by the capture or emission rates of deep traps to determine the binding energy and nature (electron or hole trapping) of the deep level.

As with any substitutionally bound hydrogenic impurity, the Cu impurity has associated with it a series of bound excited states. The bound excited states of the ground state of Cu in Ge have been investigated via infrared spectroscopy [16]. The absorption spectrum of Cu in Ge showing the ground state to bound excited state transitions is presented in Figure 1.2.

The ability of the Cu impurity to bind an extra (fourth) hole has also been observed experimentally [17]. This is due to the doubly degenerate valence band top at the Brillouin zone center. There are four hole spin states in the valence band, 3/2, 1/2, -1/2, and -3/2. The light hole and heavy hole bands are degenerate at the zone center, leading to the existence of the four hole states, two in each band. This property of the Cu impurity, as a result of the valence band degeneracy of Ge can be used as a unique tool to investigate the Metal-Insulator Transition (MIT) properties of copper in germanium.

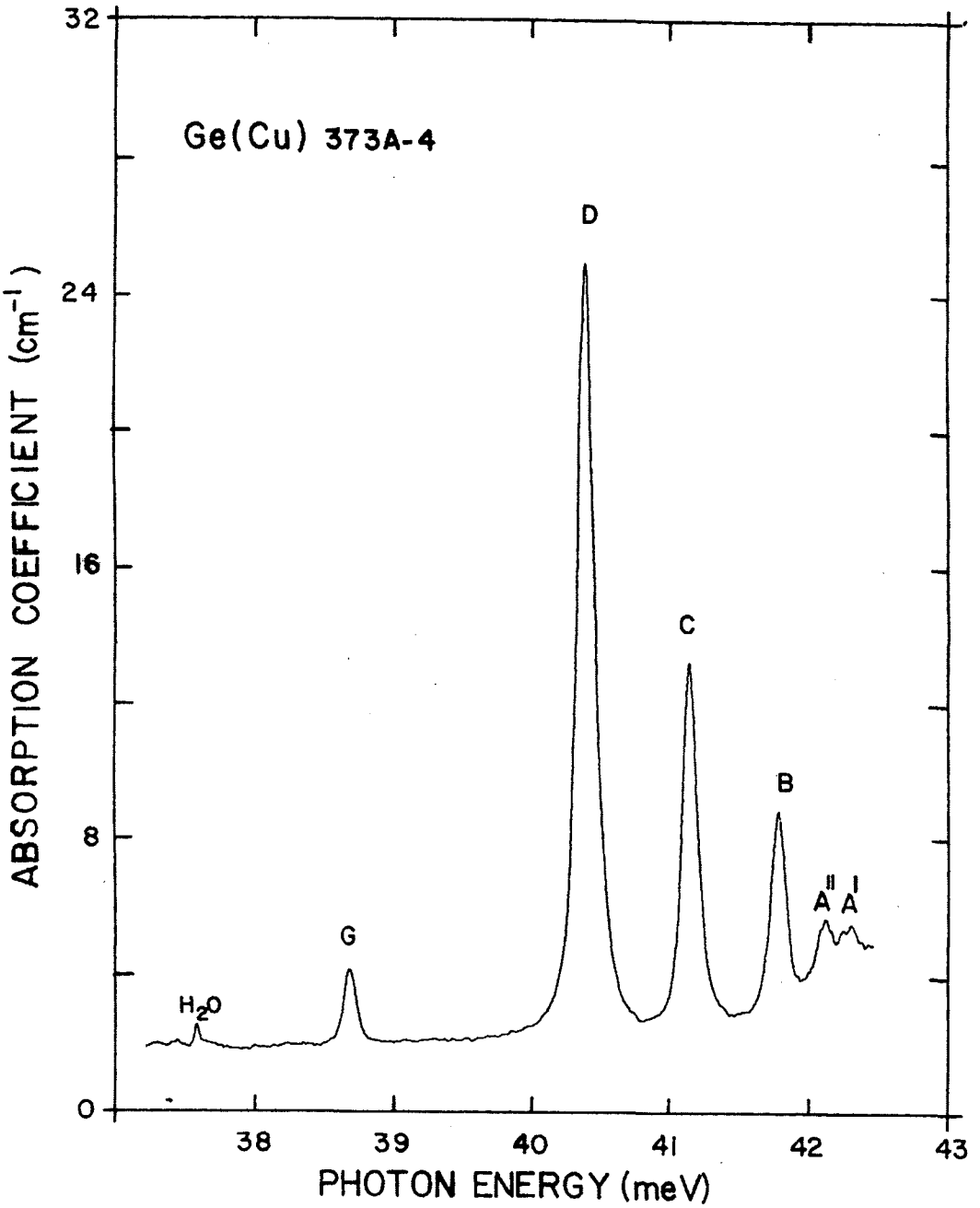

Figure 1.2 Absorption spectrum of substitutional Cu in Ge showing the ground and excited states [16].

1.1.3 Stress Effects on the Ge Bandstructure

When uniaxial stress is applied to a semiconductor crystal lattice, the lattice constant is reduced in the direction of stress causing a reduction of the symmetry of the lattice that alters the bandstructure of the semiconductor. Since the properties of the electronic states of impurities are dependent on the bandstructure, the electronic states will be altered under uniaxial stress as well.

A depiction of the energy bandstructure of Ge is given in Figure 1.3. The curves represent the allowed electron energy states in germanium as a function of crystal momentum ($\vec{k}$) with respect to the Brillouin zone. These states are determined, in part, by the periodic electrostatic potential created by the germanium atoms arranged in an ordered crystal structure (diamond cubic). The bandstructure reveals many properties of a semiconductor. Germanium is an indirect bandgap material, meaning that the conduction band minimum (L) is not found at the same value of $\vec{k}$ as the valence band maximum (Γ). The energy of this indirect bandgap is 0.67 eV at room temperature. The valence band in Ge consists of a light hole band, a heavy hole band, and a split–off band. The light and heavy hole bands are named to describe the effective hole masses which are determined from the curvature of the bands. A band with a smaller curvature will have a larger effective mass, thereby making the hole act "heavier". From Figure 1.3, it can be seen that the valence band of germanium has a doubly degenerate maximum at the Γ point of the Brillouin zone. At this point, the states of the light and heavy hole bands merge, resulting in a fourfold degeneracy of hole states at the valence band edge. The maximum of the split-

off band is located 280 meV below the valence band edge. The symmetry of these states is a Γ_8^+ representation of the double point group, O_h.

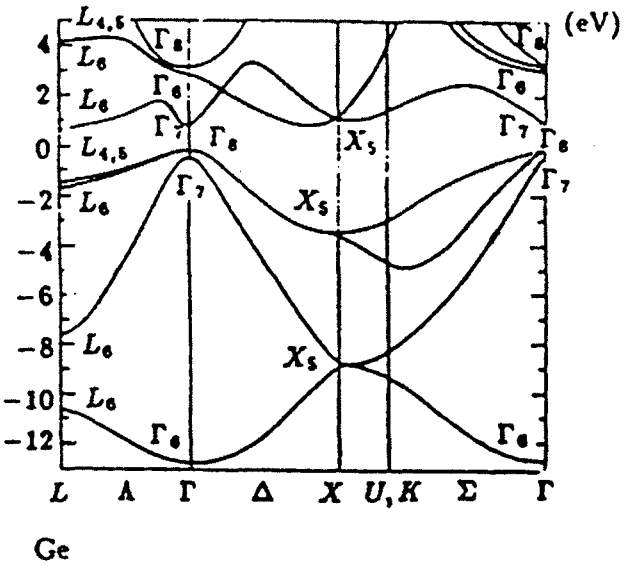

Figure 1.3 Schematic of the Ge bandstructure as a function of crystal orientation, showing allowed energy states [18].

The application of a compressive uniaxial stress in the <100> direction changes the symmetry of the crystal from the cubic O_h to the tetragonal D_{4h} point group. The representation Γ_8^+ splits into two representations, Γ_6^+ and Γ_7^+,

$$^4\Gamma_8^+\left(\overline{O_h}\right)=^2\Gamma_6^+ +^2\Gamma_7^+\left(\overline{D}_{4h}\right) \tag{1.5}$$

Therefore, the top of the valence band splits into two twofold degenerate bands. The effect on the bandstructure of the loss of symmetry and degeneracy at the valence band top was calculated by Pikus and Bir [19], and their representation of the bandstructure with and without stress effects is shown in Figure 1.4.

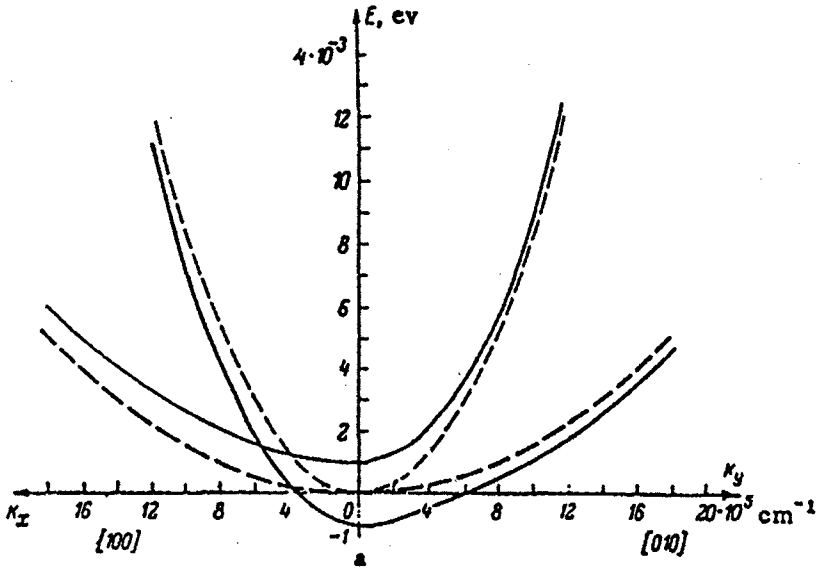

Figure 1.4 Schematic representation of the valence band maximum demonstrating the effects of a uniaxial stress applied along [100]. The dashed line is the unstressed case, while the solid line is the stressed case [19].

Since the properties of shallow acceptors are directly related to the structure of the valence band maximum, the loss of degeneracy and splitting of the valence band has a profound effect on acceptor states. For a more detailed discussion of stress effects on acceptor states, the reader is referred to Buczko [20].

1.1.4 Stress Effects on the Cu Impurity State

As noted in the previous section, the stress-induced splitting of the valence band of Ge and loss of degeneracy causes a corresponding loss of degeneracy for acceptor states. A schematic of the state splitting from a T_d symmetry into a D_{2d} symmetry created by a stress parallel to the <100> direction as well as the transitions between states is presented in Figure 1.5.

The Γ_8 ground state of the Cu acceptor splits from the symmetric $\{\Gamma_8 \times \Gamma_8 \times \Gamma_8\}$ state to two states, $\{\Gamma_6 \times \Gamma_6\} \times \Gamma_7$ and $\{\Gamma_7 \times \Gamma_7\} \times \Gamma_6$. The first bound excited state, $\{\Gamma_8 \times \Gamma_8\} \times \Gamma_8'$, splits into six states as seen in Figure 1.5. The split energy levels of the ground state and its corresponding excited states continue to separate in energy with increasing stress. This was shown by Salib, et al. [16], for Cu in Ge and is presented in Figure 1.6.

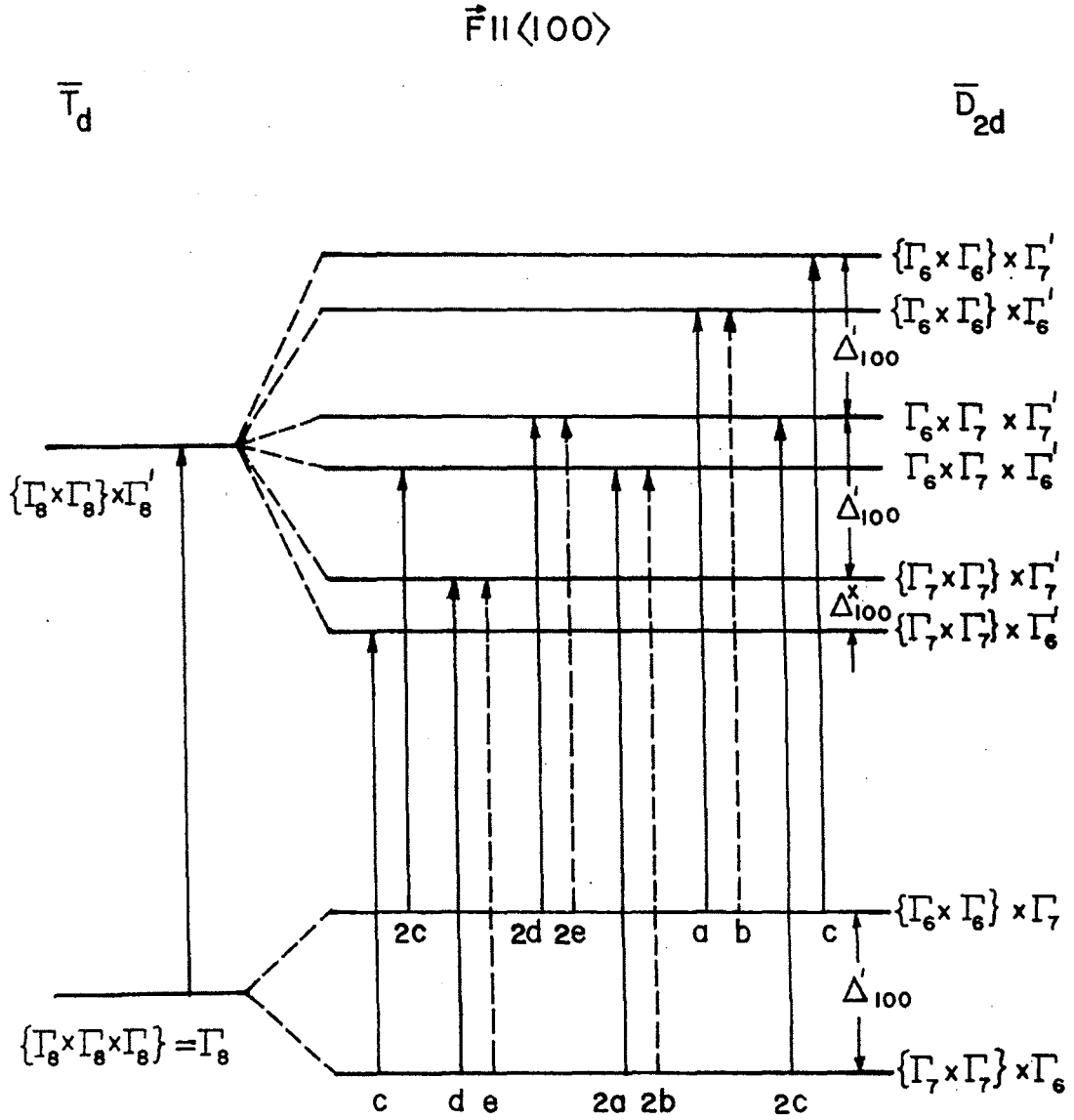

Figure 1.5 Schematic showing the changes in symmetry and state splitting under the application of uniaxial stress parallel to <100> [16].

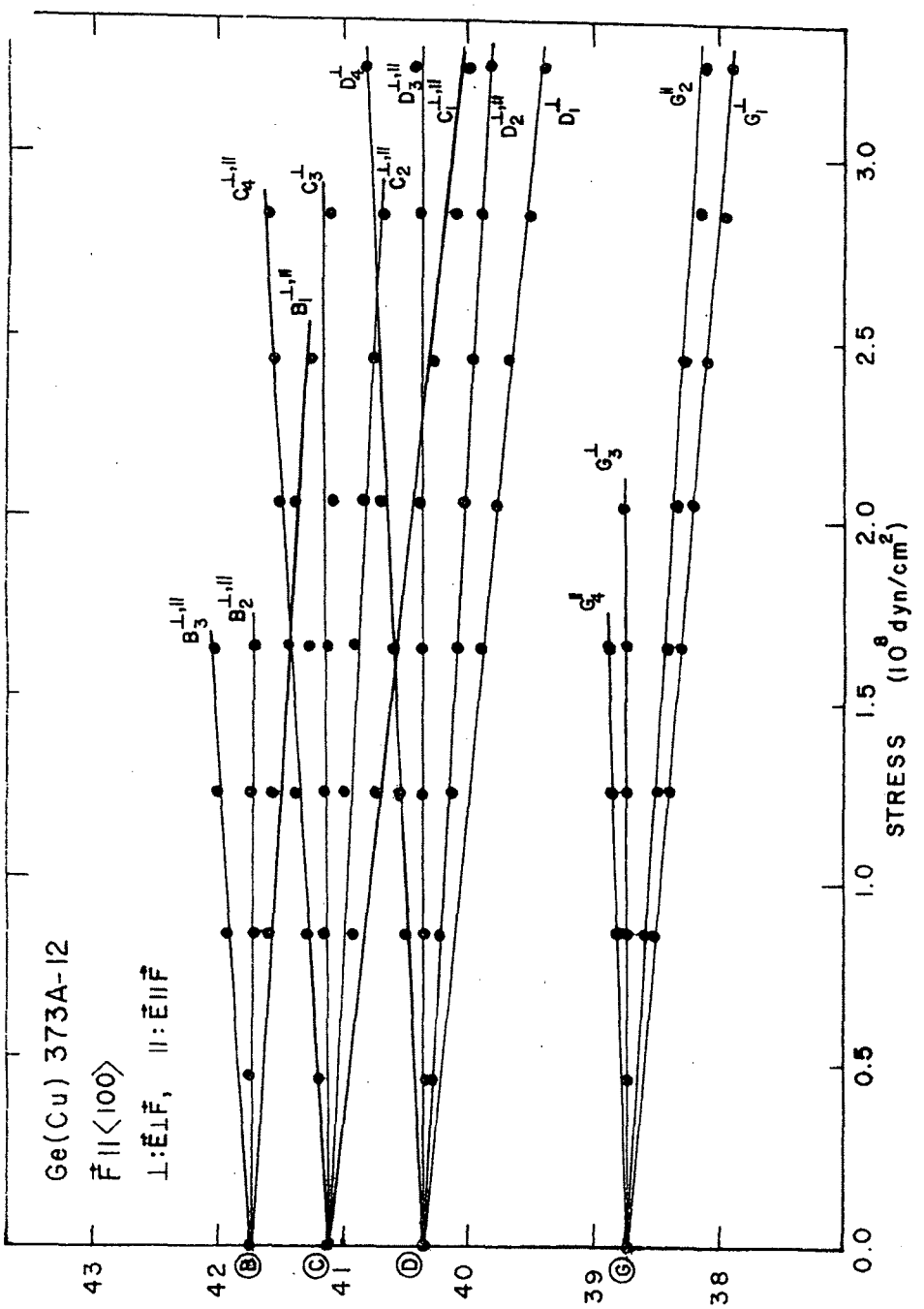

Figure 1.6 Plot of ground and excited state energies as a function of stress taken from absorption spectra. The splitting of the states under stress is evident and an increase in splitting with stress is observed [16].

1.2 Motivation for the Current Work

An interesting property of Cu in Ge is that under the application of uniaxial stress, the Cu ground state undergoes a transition from a $1s^3$ to a $1s^22s^1$ configuration [21]. This occurs because the valence band top is no longer degenerate. The third hole bound to Cu will be placed in the larger 2s orbital. By having a more extended wavefunction, the electronic states of Cu will overlap and cause the Ge to undergo a Metal-Insulator Transition at a much lower impurity concentration than previously observed with other impurities.

The Metal-Insulator Transition is a phenomenon that has been studied in a variety of materials for decades [22]. There have been difficulties in studying the MIT in doped semiconductors due to the nature of the impurity states. Shallow hydrogenic impurities have larger wavefunctions, and the impurity band that is formed at high dopant concentrations ($> 10^{17}$ cm^{-3} for Ga-doped Ge) will sit so close to the band edge that distinguishing conduction through the impurity band from "band edge" conduction becomes difficult experimentally. Deeper impurities have smaller wavefunctions, requiring a higher concentration of impurities to achieve overlap and band formation. Typically, deep-level impurities have lower solubilities than shallow-level impurities and an MIT may not be reached.

Uniaxially stressed Cu-doped Ge has been shown to be an ideal system for studying the Metal-Insulator Transition in doped semiconductors. It is a relatively deep impurity (~17 meV, under stress) with a large wavefunction due to the ground state transformation to a $1s^22s^1$ state. This allows observation of the upper and lower Hubbard bands isolated from each other as well as both the valence and conduction bands.

1.2.1 Electrical Conduction in Semiconductors

Electrical conduction in extrinsic semiconductors can be represented by an equation of the following form [23]:

$$\sigma = \sigma_1 e^{\frac{-\varepsilon_A}{kT}} + \sigma_2 e^{\frac{-\varepsilon_2}{kT}} + \sigma_3 e^{\frac{-\varepsilon_3}{kT}} \qquad (1.6)$$

where σ is the total conductivity of the semiconductor. The first term on the right side of the equation is due to the conductivity of free carriers excited from bound impurity states within the band gap to the valence or conduction band. The pre-factor, σ_1, is the conductivity of the free carriers within the valence or conduction band. It is the product of the concentration of free carriers in the band, the charge on the carriers, and the mobility of the carriers within the band. The exponential part of the first term in the above equation describes the temperature dependence of the excitation of carriers from the bound ground state to the corresponding band. The parameter ε_A is the activation (binding) energy of the impurity, k is Boltzmann's constant and T is the temperature in degrees Kelvin.

The third term in Equation 1.6 describes the conductivity of a semiconductor due to the hopping of charge carriers through isolated impurity states within the bandgap. When the conductivity due to the first term of Equation 1.6 (band conduction) is limited due to freeze-out of carriers from the band at low temperatures, hopping conductivity may dominate the total conductivity. In order for hopping between isolated states to occur, there must exist some unfilled impurity states for the carriers to move into. At low temperatures the only unfilled states will be due to compensation of majority impurity states by minority

impurities. The pre-factor of the third term, σ_3, is proportional to the probability for a hopping transition [24],

$$\sigma_3 \propto \left| \int \Psi^i \Psi^j dr \right|^2 \tag{1.7}$$

where $\Psi^{i,j}$ is the radially dependent part of the impurity wavefunction. This pre-factor describes the overlap of the wavefunctions. The exponential part of the third term in Equation 1.6 is similar in form to the first term, with ε_3, the hopping activation energy, corresponding to the shift of the Fermi energy due to Coulomb interactions among impurity states.

The second term in Equation 1.6 corresponds to conductivity from an impurity band within the bandgap of the semiconductor. An impurity band will form within a semiconductor when the concentration of impurities is such that the impurity wavefunctions overlap allowing for carriers to move through the crystal without the need for excitation to the conduction/valence band. This transport is achieved through the banded delocalized impurity states.

The exponential part of the second term is similar in form to that of the other two parts, with the activation energy, ε_2, representing the energy required to place an additional charge carrier on an impurity by overcoming the Coulomb repulsive energy of the carriers already present on the impurity site. The activation energy is on the order of a few meV, and decreases as the impurity concentration increases.

1.2.2 Impurity Conduction via Hubbard Bands

The impurity conduction in heavily doped semiconductors occurs via a system of two impurity bands referred to as Hubbard bands. They are so named because of the way

these bands form. The bands develop when the concentration of impurities reaches a concentration at which the wavefunctions of the impurities begin to overlap significantly. J. Hubbard described the interaction of the states of the neighboring impurities by creating a simplified model [25]. In his model he reduces all of the states of the electrons bound to an impurity to a single localized level. He then gives four possible states for the impurity level: it can be empty, contain one electron of either of two spin orientations, or contain two electrons of opposite spin. Of interest to our studies is the case where the level contains two electrons of opposite spin, obtaining one of the electrons from a neighboring impurity. To be placed on the same impurity, the second electron must have a positive energy U in order to overcome the electrostatic Coulomb repulsion of the electron initially present on the impurity. This second electron occupies a state that is offset from the first electron state by the energy U, known as the Hubbard gap energy. This second electron is said to be in an overcharged state, while the first electron is in a ground or neutral state. The overcharged state, due to the positive energy U, is not tightly bound. This gives rise to a highly delocalized state, which forms a band (upper Hubbard band) of highly mobile carriers within the bandgap when the interactions of all of the impurities are taken into account. The lower Hubbard band is formed by the collection of neutral charge states.

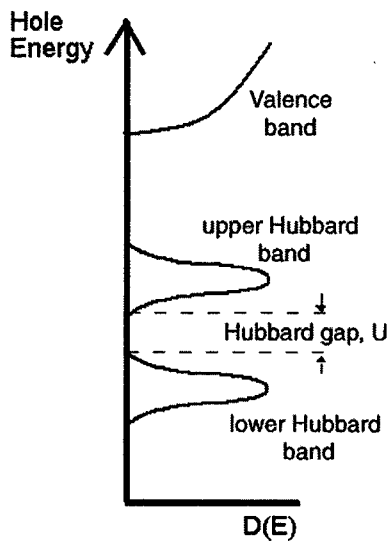

Figure 1.7 Schematic of the density of states for a Hubbard band system of acceptor impurity states. The two Hubbard bands are shown here well separated from the valence band for clarity.

The overlap of impurity wavefunctions and impurity band formation within a semiconductor is a manifestation of the Hubbard model. A schematic representation of a Hubbard band system formed from acceptor states is presented in Figure 1.7. This representation has been simplified to demonstrate the various parts of an impurity band based on the Hubbard model. For shallow acceptors in a heavily doped semiconductor, exchange of holes between impurity states via the Hubbard model will result in the formation of the upper and lower Hubbard bands. Due to its formation from the neutral shallow acceptor states, the lower Hubbard band is located at the same energy as the shallow acceptor. The upper Hubbard band will be offset from the lower Hubbard band toward the valence band by the Hubbard gap energy, U. It is this offset from the shallow acceptor energy that places the upper Hubbard band at or near the valence band edge.

1.2.3 Stress-Induced Ground State Transformation in Ge:Cu

One of the more unique properties of copper in germanium is the recently discovered ground state transformation that occurs under the application of uniaxial stress [21]. As discussed in the previous section, the application of stress breaks the symmetry of the valence band in Ge. The valence band changes from the degenerate Γ_8 (O_h symmetry) band to two bands, Γ_6^+ (D_{4h}) and Γ_7^+ (D_{4h}). The shallow acceptor state wavefunction consists of wavefunctions describing the valence band. They undergo a change in symmetry due to the splitting of the valence band. The acceptor state symmetry changes from T_d to a D_{2d}. Because of the valence band's splitting into Γ_6 and Γ_7 bands, the copper levels split into $1s(\Gamma_6)$ and $1s(\Gamma_7)$ states. This is shown schematically in Figure 1.8.

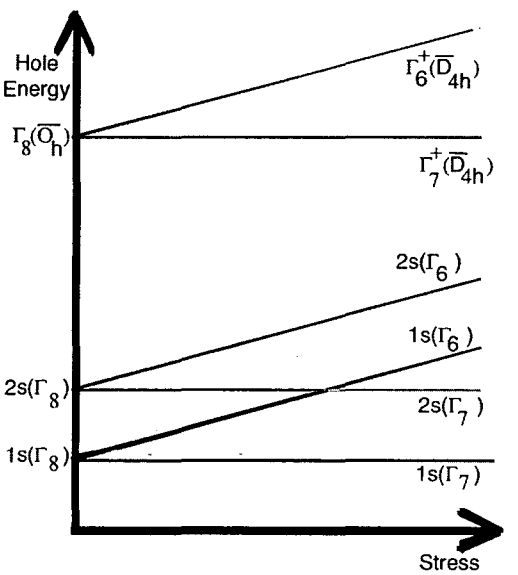

Figure 1.8 Schematic representation of the Cu acceptor state splitting, showing the crossing of the $1s(\Gamma_6)$ and $2s(\Gamma_7)$ states.

Figure 1.8 also demonstrates an interesting effect of stress on an acceptor that binds more than two holes, such as Cu. The $1s(\Gamma_7)$ level will accommodate two holes, with the third hole residing in the $1s(\Gamma_6)$ level. As the stress increases, the $1s(\Gamma_6)$ and $1s(\Gamma_7)$ acceptor levels continue to split with the $1s(\Gamma_6)$ level increasing in energy. At some point, the $1s(\Gamma_6)$ level crosses with the bound excited state $2s(\Gamma_7)$, the lower part of the 2s level which has split into corresponding $2s(\Gamma_6)$ and $2s(\Gamma_7)$ levels. Once the $1s(\Gamma_6)$ level has crossed the $2s(\Gamma_7)$ level, the ground state of copper reconfigures itself from a $1s^3$ state, $[1s(\Gamma_7)]^2[1s(\Gamma_6)]^1$, to a pseudo Li-like state of $[1s(\Gamma_7)]^2[2s(\Gamma_7)]^1$, with the third hole dropping from the$1s(\Gamma_6)$ level to the now lower $2s(\Gamma_7)$ level. This reconfiguration leads to a lower energy configuration at the elevated stress levels and more stable.

This reconfiguration of the Cu ground state was verified by measuring the photoconductive response spectra of Ge:Cu under increasing stress. Some of the spectra are shown in Figure 1.9.

A shift in the onset of the first ionization potential of Cu with increasing stress can be seen in the spectra of Figure 1.9. This onset was measured for a series of stress values and plotted in Figure 1.10. The Cu binding energy decreases under stress from a zero stress value of 43 meV to a value of 17 meV. The stress dependencies of the ionization potentials of the two ground state configurations, $1s^3$ and $1s^22s^1$, were calculated and are also plotted in Figure 1.9 as solid lines. At low stress, the binding energy of the Cu impurity follows the calculated stress dependence of the $1s^3$ ground state binding energy. Above a stress of 4 kbar, the Cu binding energy switches to that of the stress independent $1s^22s^1$ ground state. The $1s^22s^1$ ground state was found to have a binding energy of 17 meV.

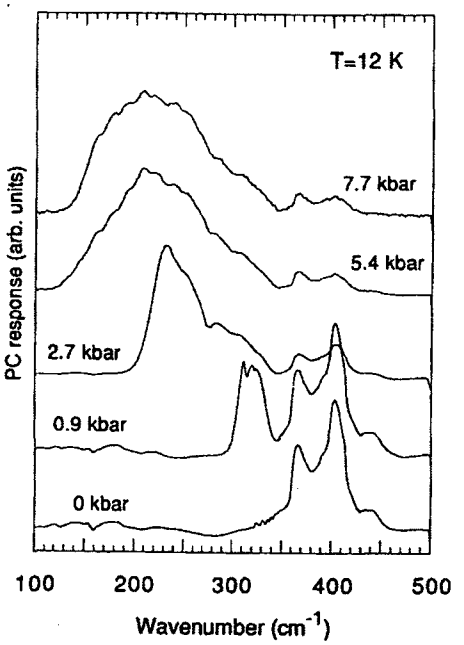

Figure 1.9 Photoconductivity spectra of Cu in Ge under increasing uniaxial stress. A shift in the onset of the Cu response, corresponding to the binding energy of Cu, can be seen with increasing stress [21].

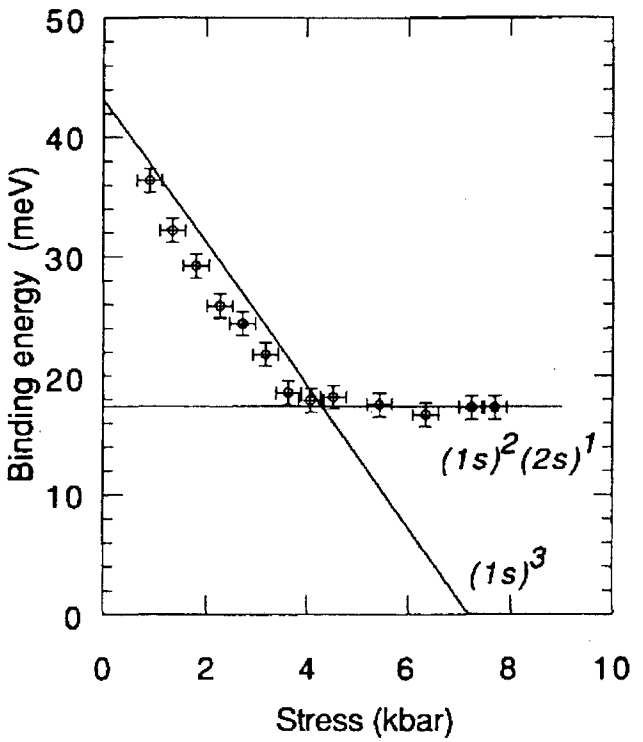

Figure 1.10 Plot of Cu binding energy, taken from photoconductivity spectra, versus stress. Solid lines are the calculated dependencies of the binding energy with stress [21].

The observed ground state transformation under stress and the resulting occupation of the 2s state have profound implications for impurity band formation and conduction, because both properties depend on the size of the impurity wavefunction. The next section describes in detail the implications of the Cu ground state transformation and how it can be used to study Metal-Insulator Transitions in Ge.

2 Hubbard-band Conduction in Ge:Cu

2.1 Formation of Hubbard bands in Ge:Cu

Previous work on Hubbard band conduction in germanium focused on shallow impurities because their large wavefunctions led to overlap already at moderate concentrations [26]. The impurity conduction of copper in germanium was studied previously, and the extent of the Cu ground state wavefunction was determined to be about half that of shallow impurities [27]. This can be a disadvantage when trying to form impurity bands due to the reduced overlap. However, by applying uniaxial stress and causing the ground state transformation discussed above, the Cu acceptor uniaxially stressed Ge offers the combined advantage of a deep impurity (separation from the valence band) with an extended wavefunction (2s state).

The Hubbard bands in Cu-doped Ge are formed in the same manner as in any other semiconductor. The Cu atoms are diffused into the crystal and are dispersed randomly throughout the lattice at substitutional positions. If the concentration of Cu atoms is high enough, the Cu wavefunctions will overlap and Hubbard bands will form.

The difference between Ge:Cu and semiconductors highly doped with shallow impurities has to do with the size of the Cu acceptor wavefunction under uniaxial stress and its occupation by three holes. By applying stress to the crystal and splitting the degeneracy of the valence band, the copper levels will split, and at a high enough stress the copper will undergo a ground state transformation from a $1s^3$ state to a $1s^2 2s^1$ state. This is shown schematically in Figure 2.1.

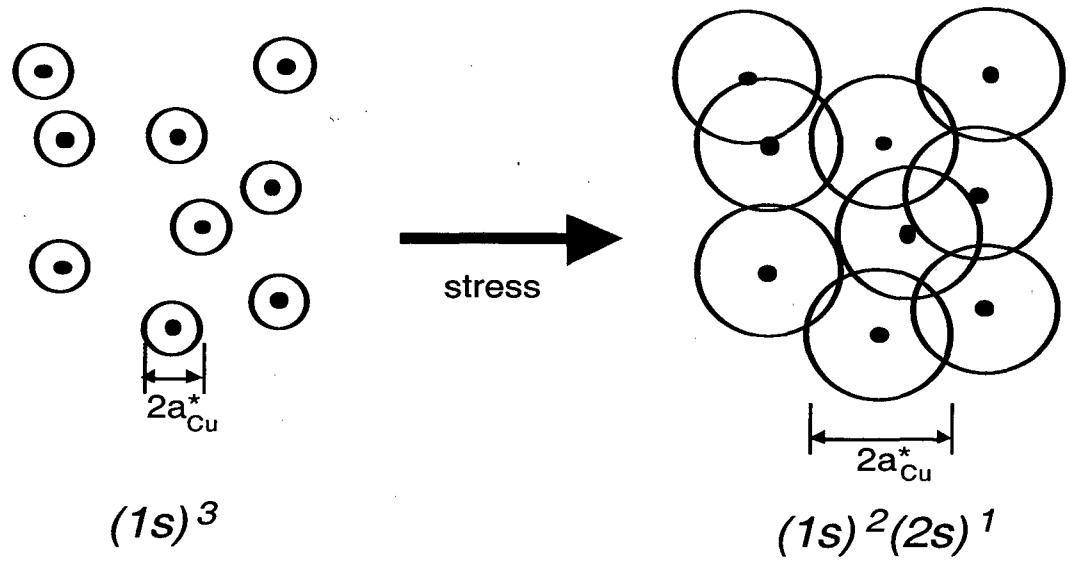

Figure 2.1 Schematic diagram of the effect of the stress-induced ground state transformation on wavefunction overlap [28].

This results in a larger wavefunction (19.2 nm) for the holes bound to the copper. Hubbard band formation will then occur at a lower concentration for Cu-doped Ge than for shallow impurities in Ge, according to the Mott condition for a MIT [22]:

$$n^{1/3}a_H = 0.25 \qquad (2.1)$$

Where n is the critical concentration for a Metal-Insulator Transition (MIT), and a_H is the size of the wavefunction.

The benefit of this is that the two bands, the upper and lower Hubbard bands, have narrower density-of-state functions and are less broad than a set of bands in a more heavily doped semiconductor (See Figure 2.2). The weak broadening leads to the two bands (See Section 1.2.2) being well separated from each other. This, in turn, makes studying the properties of the two bands much easier.

2.2 Observation of a Metal-Insulator Transition

A Metal-Insulator Transition can be achieved in stressed Ge:Cu by increasing the copper concentration in the crystal to the critical concentration. As the copper concentration increases, the activation energy, ε_2, for excitation from the lower to upper Hubbard band decreases. This energy, the Hubbard gap energy, is the energy required to overcome the Coulomb repulsion of the carriers on an impurity site by the addition of an extra carrier. When the Hubbard gap energy reaches zero, there is no activation energy required for carrier transport, and the non-localized states become metallic in nature. It is in this manner that the uniaxially stressed Ge:Cu undergoes a Metal-Insulator Transition. This transition is shown schematically in Figure 2.2, where the increase in concentration has led to a broadening of the density of states and a merging of the upper and lower Hubbard bands.

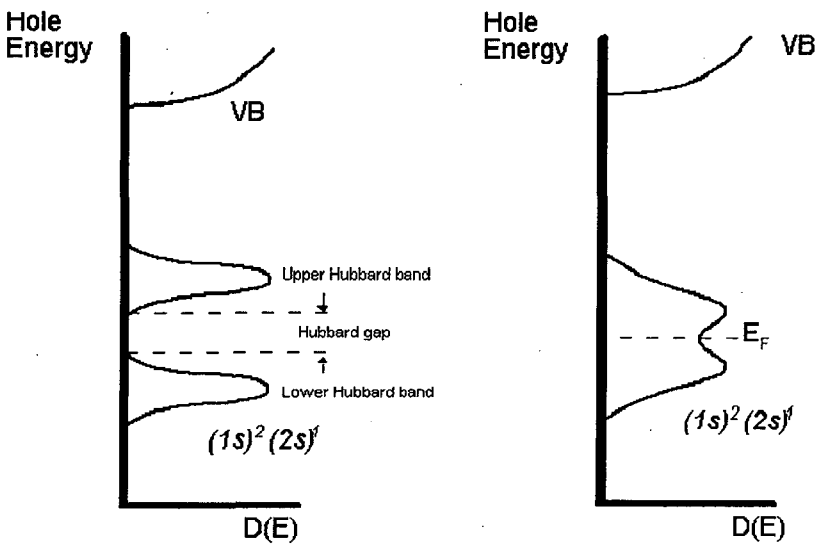

Figure 2.2 Schematic of the density of states for the uniaxially stressed Ge:Cu system, below the MIT (left) and above the MIT (right).

By measuring the free carrier concentration of uniaxially stressed Ge:Cu as a function of temperature via the Hall effect for varying Cu concentrations, the reduction of the Hubbard gap energy and the MIT can be observed. Samples with copper concentrations ranging from 3×10^{14} cm^{-3} to 1.6×10^{16} cm^{-3} were measured [29]. The results of the Hall effect measurements are presented in Figure 2.3 and 2.4.

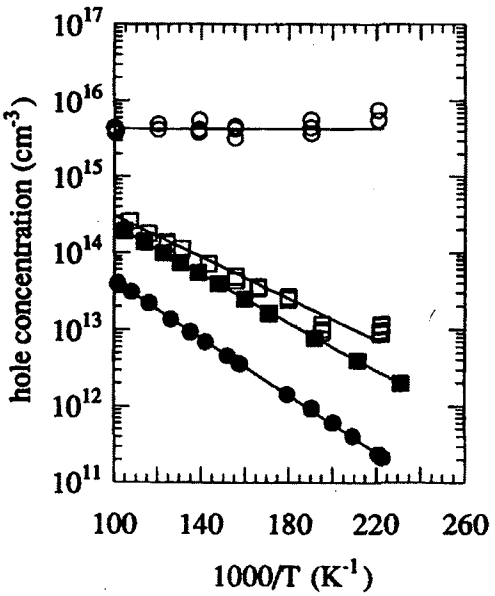

Figure 2.3 Hole concentration versus 1000/T for Ge doped with Cu concentrations ranging from 3×10^{14} cm^{-3} to 1.6×10^{16} cm^{-3}, as measured by Hall effect [29].

The Hubbard gap energy can be derived from the slopes of the curves in Figure 2.3. The slopes are given by ε_2/k, where ε_2 is the Hubbard gap energy, and k is Boltzmann's constant. These values are plotted in Figure 2.4.

The solid line in Figure 2.4 is a calculation of the Hubbard gap energy using a Li atom to model the Cu atom, which has a Li-like ground state under stress. The model yielded the following equation for the Hubbard gap energy [29],

$$\Delta = \mu E_B \left[0.49 - 352 N_{Cu} \left(a_B / \mu \right)^3 \right] \tag{2.2}$$

Where Δ is the calculated Hubbard gap energy, μ is a parameter which gives the size of the hole wavefunction, E_B is the Cu binding energy, N_{Cu} is the Cu concentration, and a_B is the effective Bohr radius. The curve plotted in Figure 2.4 uses a μ of 1.3, E_B of 17 meV, and an a_B of 6.4 nm. The calculated Δ is about 16% higher than the experimental data at low Cu concentrations. The calculation is an approximation and does not include any electron-electron correlation. For hydrogenic impurities, the electron-electron correlation is known to reduce Δ by about 24%. The calculated line verifies that a Hubbard gap does exist in this system and that increasing the Cu concentration can induce an MIT.

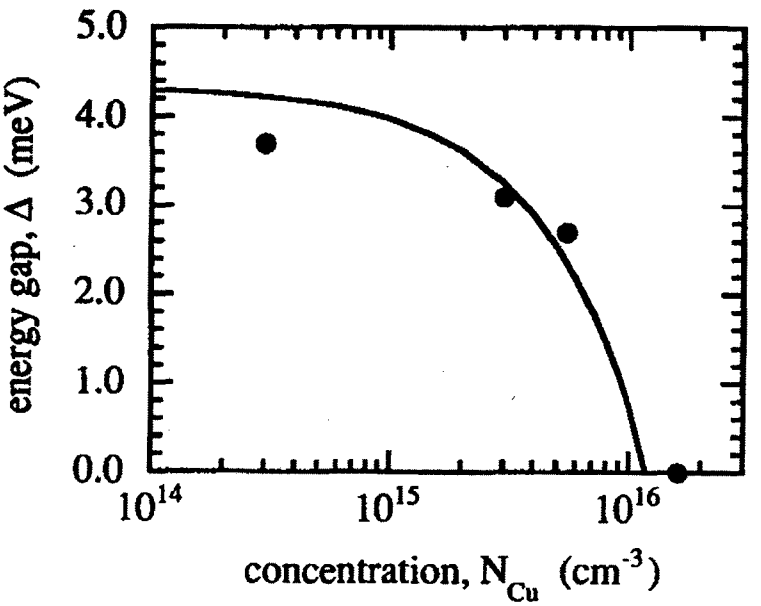

Figure 2.4 Hubbard gap energy versus Cu concentration in Ge, showing a closing of the Hubbard gap and an MIT. The solid curve is a calculation from Equation 2.2 [29].

It has been demonstrated that an MIT can be observed in uniaxially stressed Ge:Cu by increasing the Cu concentration sufficiently. Liu et al. [30] reported a similar closing of the Hubbard gap with increasing impurity concentration for uncompensated heavily doped Si:P using thermoelectric power and resistivity measurements. Additional reports have also

been made on the observation of an MIT in a semiconductor in which the semiconductor was doped to above the MIT and a magnetic field was applied to reduce the wavefunction and separate the bands [31,32,33,34]. In the uniaxially stressed Ge:Cu system, the concentration can be tuned to control band overlap, and magnetic field tuning is not necessary.

3 Experimental

In order to perform the electrical measurements for this research, ultra-pure single crystal germanium samples were chosen as the starting material. They were cleaned and equipped with ion implanted and metallized contacts. For some of the experiments, the samples were placed under a uniaxial stress to induce the ground state transformation described in Section 1.3.3. This section details the sample processing and the application of stress required for the experiments performed.

3.1 Sample Preparation

All of the copper doped germanium samples used in the experiments were processed in the same manner. For samples with residual shallow n-type or p-type dopants the only difference was the as-grown impurities of the starting Ge material used for copper diffusion. The starting material was chosen based on type and concentration of shallow dopants necessary for the desired experimental application.

In order to prepare the samples for Cu diffusion, 1-mm thick wafers were cut from Czochralski grown single crystals of Ge oriented along the <100> direction. The wafers were then cut into 8-mm wide strips using a dicing saw such that all faces of the resulting pieces were <100> oriented. All of the surfaces were lapped with 600-μm and 1200-μm grit slurries, in succession. The samples were then etched in a 3:1 $HF:HNO_3$ solution for 90 seconds to remove surface damage due to the cutting and lapping steps. A 200-nm thick layer of Cu was Ar sputtered on one of the larger sample surfaces. The Cu sputtered samples were sealed individually in quartz ampoules under half an atmosphere of argon. The argon is added to the ampoule to allow for better thermal coupling between the sample

and the quartz. The improved thermal coupling aids in quenching the samples. This is important because the samples must be quenched as quickly as possible in order to freeze the Cu atom population, existing at high temperatures, into the substitutional positions.

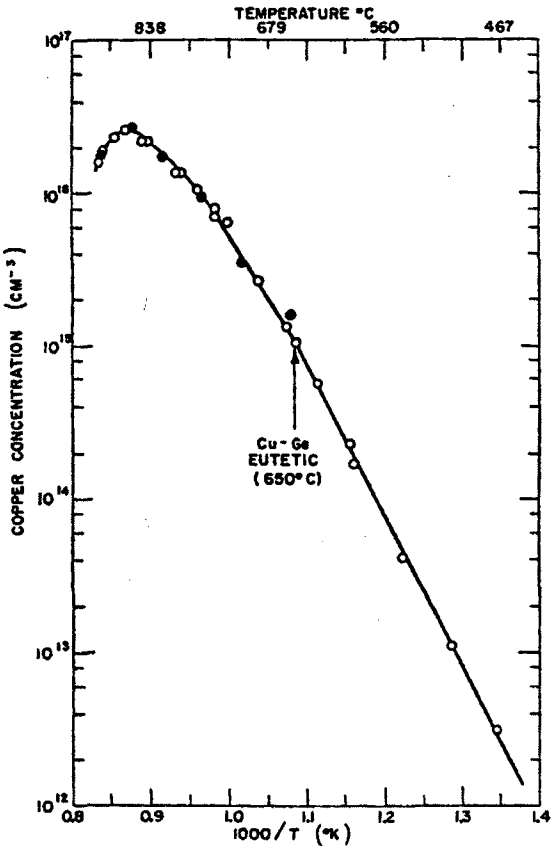

Figure 3.1 Substitutional copper concentration in Ge as a function of inverse temperature [6].

Once the sample is sealed in the ampoule, it is placed in a vertically mounted furnace and heated to the desired temperature for 24 hours. The annealing temperature was chosen based on the solubility of substitutional Cu in Ge at elevated temperature determined by Woodbury and Tyler and presented in Figure 3.1. The samples were heated to the temperature corresponding to the desired concentration given by Figure 3.1.

The furnace is mounted vertically to allow the ampoule to be dropped directly into a bath of ethylene glycol. This step is taken to minimize the quench time as much as

possible. The sample is heated for a sufficient amount of time to allow the Cu to diffuse evenly throughout the crystal. Copper is a rapid diffuser in Ge and would not need the full 24 hours to diffuse throughout, however ample time was given to ensure a homogeneous distribution in all of the samples.

After removing the sample from the ampoule, it was prepared for the electrical characterization measurements. First, the samples are lapped and etched according to the method described above to remove any residual Cu from the surface. The two opposing large flat surfaces are ion implanted with boron (25 keV/1 $\times 10^{14}$ cm^{-2} and 50 keV/2 $\times 10^{14}$ cm^{-2}) to create p^+ contacts. On top of the implanted surfaces, a 40 nm thick layer of Pd is deposited along with a 400-nm thick layer of Au on top of the Pd using Ar sputter-deposition. The samples were annealed at 300 °C for one hour to activate the implanted boron, repair implantation damage and react the Pd with the Ge surface to form Ohmic contacts.

An 8 × 8-mm^2 sample was cut from each copper diffused and metallized wafer of Ge, for use as a Hall effect sample. In order to form the contacts for the Van der Pauw geometry Hall effect measurements, one 8 × 8 mm^2 surface and all of the 1 × 8-mm^2 sides were lapped (as above) to remove the metal and implant layers. The other 8 × 8 mm^2 surface had the corners masked with tape to protect them from the etchant. The sample was etched in a KBr solution for 1 minute to remove the metallized layer followed by a 3:1 $HF:HNO_3$ solution (30 seconds) to remove the implanted Ge surface. The tape is then removed to reveal the four isolated contacts on the corners. Wires were connected to the four contact areas of the Hall effect samples using a conductive epoxy (Epo-Tek H20E) and 30 gauge insulated wires.

To make samples for the low temperature stressed resistivity measurements, 1×1 mm^2 squares were cut from the metallized wafers creating $1 \times 1 \times 1$ mm^3 cubes with all sides <100> oriented, and two opposing sides containing the Ohmic contacts. The cubes were then etched in the 3:1 $HF:HNO_3$ solution (1 minute) to remove the surface layer that was damaged in the cutting process.

3.2 Application of Stress

As previously discussed (Sections 1.3.3 and 2.3), in order to observe the ground state transformation and Hubbard band formation in Ge:Cu, uniaxial stress must be applied along the <100> direction. For these experiments, a leaf-spring stressing apparatus, used to stress infrared detectors for space astronomy applications, was used [35]. A schematic of the stress rig is presented in Figure 3.2.

Stress is applied to the sample, (position **f** in Figure 3.2), by turning screw **a**. This deflects the leaf spring, **b**, by an amount **d**. Because of the fulcrum at position **c**, the opposite end of the leaf spring applies a force on piston **g**. Since position of the second piston is fixed by screw **h**, the force applied by the leaf spring to the pistons is transferred to the sample as a uniaxial stress upon the crystal.

The amount of stress applied can be determined in two ways. The stress can be calculated from the deflection of the leaf spring, or by comparing the percent change in resistance of the sample to a plot of percent change in resistance versus applied stress generated by a previously calibrated germanium sample.

The stress can be calculated by using the equations for elastic bending of beams. The force, F, is transferred to the sample through the piston, as a result of the deflection, δ, of the leaf spring. The leaf spring is simply a beam that is deflected by the turning of a

screw. The stress can be calculated directly from material parameters and dimensions of the stress rig for a given rotation of the screw. This is seen in the following equation that describes this relationship:

$$F = \frac{nwEt^3\delta}{l^3} \tag{3.1}$$

In this equation, n is the number of leaf springs, w is the width of the spring, t is the spring thickness, E is Young's modulus for the spring, and l is the effective spring length, which is the distance along the spring between the two pistons.

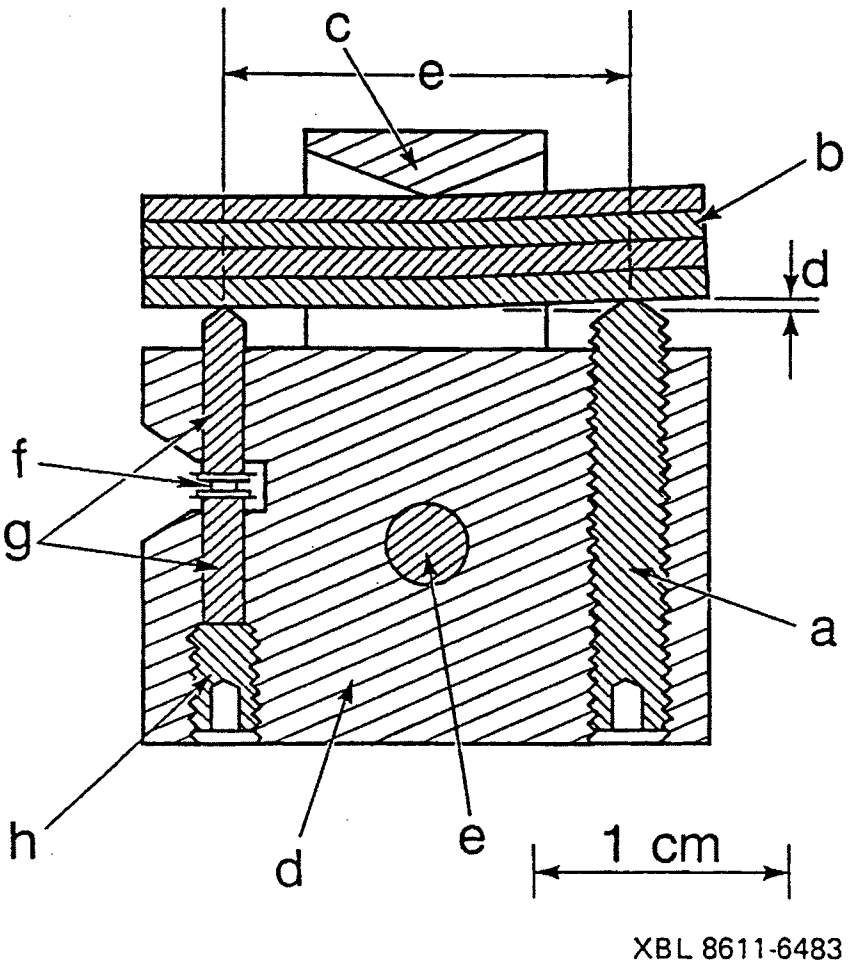

Figure 3.2 Cross section of the leaf spring stressing apparatus used to apply uniaxial stress to Ge:Cu samples: a) carbon steel screw, b) leaf springs, c) fulcrum saddle, d) stainless steel support, e) steel pin holding fulcrum, f) Ge:Cu sample, g) drill rod pistons, and h) carbon steel screw [35].

The standard leaf springs used in the stress rig are made of phosphor-bronze and have dimensions of, w = 4.6 mm, t = 2.1 mm, and l = 15.5 mm. In most cases two leaf springs are used. Given that the Young's modulus for phosphor-bronze is 1.1×10^{-4} kg/mm^2, and that the required force to generate the ground state transformation is ≥ 40 kg/mm^2, Equation 3.1 for these parameters yields, $\delta = 0.174$ mm. So for these parameters, the spring must be deflected 0.174 mm to achieve a stress of ≥ 40 kg/mm^2. Carbon steel 4-40 screws were used in the stress rig, meaning that one turn of the screw would lead to a 1/40" (0.64 mm) deflection in the spring. The screw should be tightened 0.27 turns (1/3 of a turn was used as a safe approximation), to insure that at least 40 kg/mm^2 is applied to the sample.

The calculation of stress was performed as an exercise to verify the experimental results. The stress was not calculated for each sample; rather, the percent change in room temperature resistance with applied stress was measured and compared to the data in Figure 3.3. Figure 3.3 is the plot of percent change in resistance versus applied stress for a Ge:Ga sample that was used as the calibration to determine the stress applied to the Ge:Cu samples. Due to the contraction of the stress rig materials upon cooling, the stress is expected to increase slightly. However, since the Cu binding energy is independent of stress over a threshold value of 4.2 kbar, the stress was set above the threshold at room temperature and a determination at LHe temperatures was no longer necessary.

Resistance measurements under the applied stress were used not only to determine the amount of stress applied but many of the properties of the Hubbard bands as well. To measure the resistance of the sample, current is passed and the voltage is measured through one pair of Ohmic contacts previously deposited on opposing sides (see section 3.1). In order to observe the desired stress induced effects on the crystal, the resistance was

measured in the direction of applied uniaxial stress. Because of this need, wire contacts would have to be made to the same 1 mm^2 surface that the stressing pistons would be in contact with. Such a geometry creates two problems. First, the pistons must press flat against the sample surface in order to apply uniform stress to the crystal, meaning the wire can not be placed on the stressing surface. Secondly, if the wire and piston contact the same surface, the contacts will be electrically shorted to the stress rig frame. To alleviate both of these problems, electrical contact was made to the metallized surface by means of wires soldered to thin brass shims.

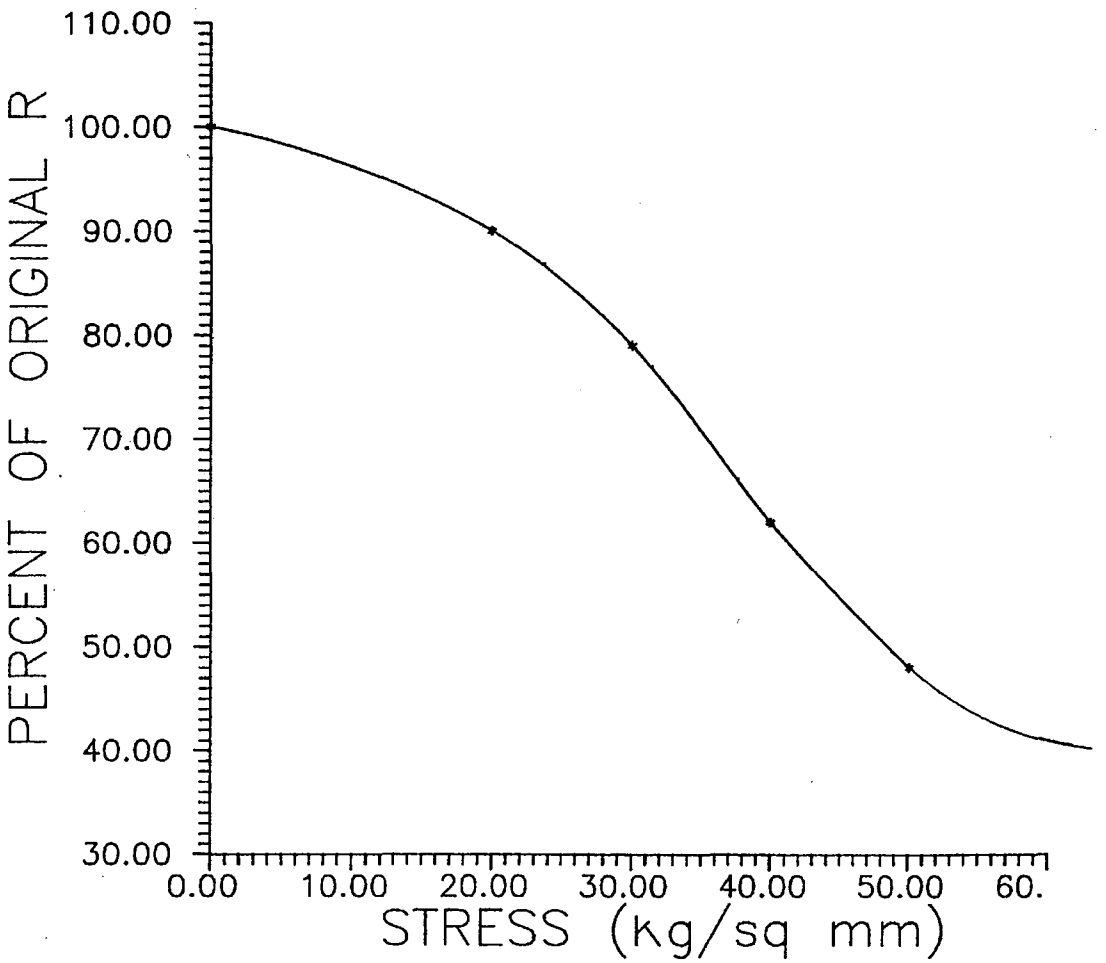

Figure 3.3 Plot of percent change in resistance vs. stress for a Ge:Ga sample [35]. This plot was used to determine the level of stress in a Ge:Cu sample.

These brass shims were then placed on the metallized surface to be stressed. Thin 1-mm diameter circular sheets of mica were attached to the piston heads to insulate the sample from the stress rig. By using thin sheets of brass and mica, wires could be contacted with the sample remaining insulated while maintaining planar and parallel surfaces for the application of stress.

4 Uniaxially Stressed Germanium Doped with Cu and Shallow Donors

4.1 Introduction

As discussed in Section 1.2.2, the lower Hubbard band is formed by neutral states of the impurities. In an uncompensated system at low temperatures, all of the states of the lower Hubbard band are filled, and no conduction can be observed in the lower Hubbard band. The only process by which conduction can take place in the lower Hubbard band is via hopping conduction through the localized states. In order to observe hopping conduction between the states of the lower Hubbard band, some states must be empty to allow carriers to move from full to empty states.

Copper acceptors were added to a shallow donor doped Ge crystal to partially compensate the Cu acceptors and thereby create empty states in the lower Hubbard band made up of Cu impurities. An energy band diagram demonstrating the compensation of the Cu impurity states by shallow donors is presented schematically in Figure 4.1. A lower energy configuration can be created if the electrons bound to the shallow donors reduce their energy by dropping down to the acceptor states and combining with a hole. By doing this they compensate the acceptor state, creating an empty state on the acceptor. It can been seen from the figure that if the dopant concentrations are selected such that the shallow donors are greater than the shallow residual acceptors, $N_D > N_A$, and the Cu concentration is greater than the net shallow dopant concentration, $N_{Cu} > N_D - N_A$, a partially compensated Cu level will be created.

Figure 4.2 is a schematic of a model density of states for the Ge:Cu:(shallow donor) system, showing the compensation of the Cu acceptor and creation of empty states in the lower Hubbard band. It is through these states that hopping should be observed.

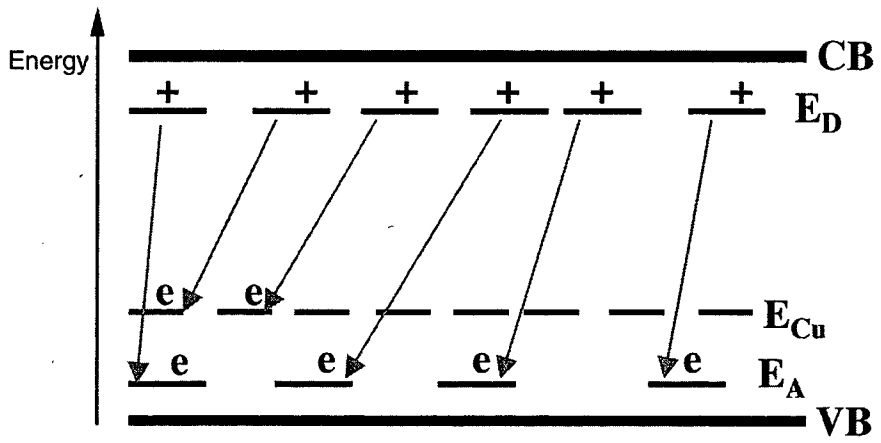

Figure 4.1 Germanium energy band diagram showing the compensation of copper and shallow acceptors by shallow donors. CB and VB represent the conduction and valence bands, respectively. E_A, E_D, and E_{Cu}, represent the energy levels of the shallow acceptors donors and Cu.

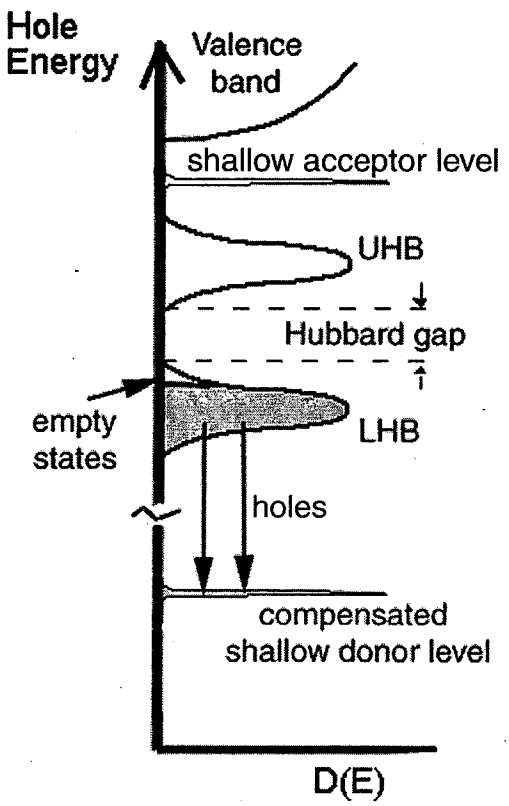

Figure 4.2 Density of states schematic for Cu and shallow donors in Ge, showing empty states in the lower Hubbard band as a result of compensation.

4.2 Experimental Approach and Results

To investigate hopping conduction in the lower Hubbard band of Cu-doped Ge, the samples were doped with Sb in order to partially compensate the Cu states. For these experiments a Czochralski-grown Sb-doped Ge crystal (#831-17.0) was used. This crystal was grown with a <100> orientation from a melt in a silica (SiO_2) crucible in a H_2 atmosphere. A wafer was cut and then Cu-diffused, at a temperature of 720 °C for 24 hours, and processed as described in Section 3.1. A Hall-effect sample was created from this material as described in Section 3.1, and a Hall-effect measurement performed in order to determine the Cu and Sb concentrations in the sample after processing.

Measurement of the Hall effect as a function of temperature yields freeze-out curves similar to that shown in Figure 4.3. By plotting the free carrier concentration vs. 1/T, an Arrhenius plot is obtained. The slope of the freeze-out yields the activation energy of the majority carrier. The curve saturates at high temperature at a free carrier concentration equal to $N_{Majority}$-$N_{Minority}$, where N_x are the majority and minority carrier concentrations, respectively. The freeze-out curve changes slope at the free carrier concentration equal to $N_{Minority}$, from a slope of $-E_A/2k$ to $-E_A/k$, where E_A is the majority carrier activation energy.

The data from the Hall effect measurement on Ge:Cu:Sb #831-17 is presented in Figure 4.3. From the saturation level of the data in Figure 4.3, the net Cu concentration, N_{Cu}-N_{Sb}, was determined to be 6×10^{15} cm^{-3}. The plot yields an Sb concentration of 3×10^{14} cm^{-3}.

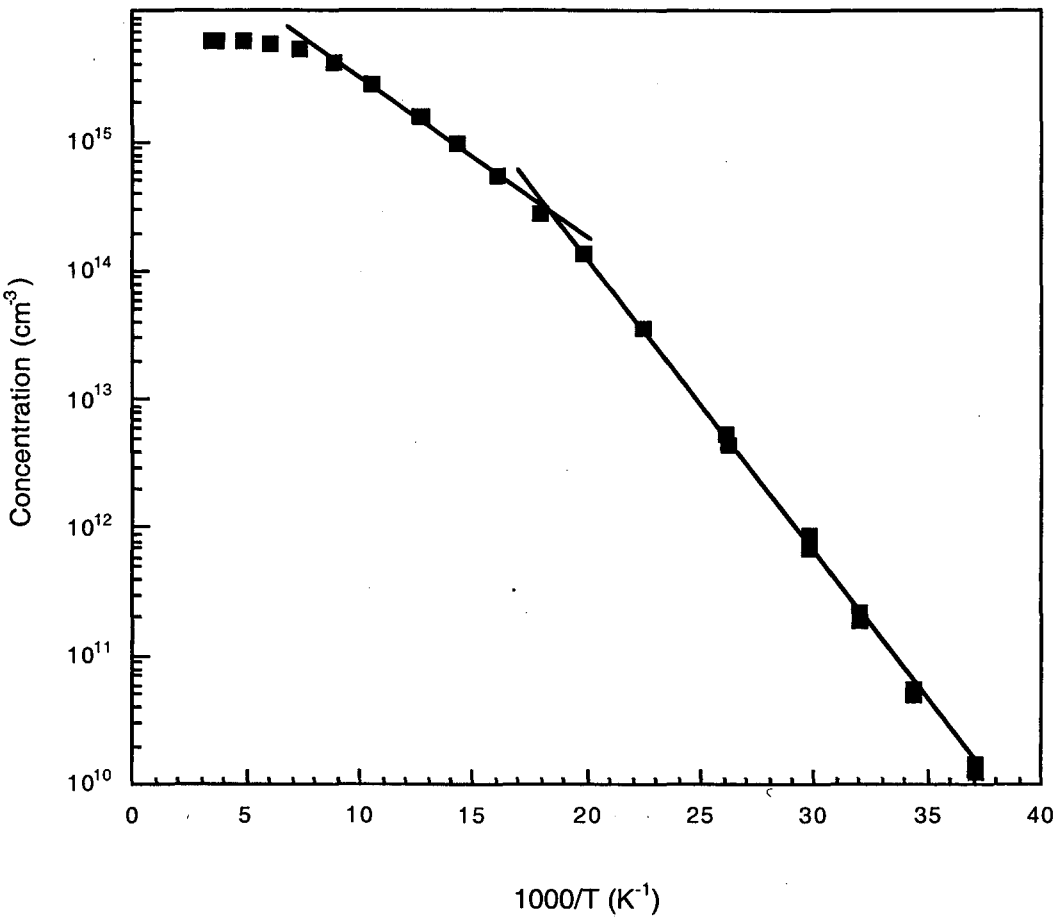

Figure 4.3 Free carrier concentration vs. 1000/T for Ge:Cu:Sb sample #831-17 determined by Hall effect. Solid lines show half slope and full slope freeze out regimes.

An unstressed 1 mm^3 cube of Ge:Cu:Sb sample #831-17 was prepared for resistivity measurements as described in Section 3.1. Ohmic contacts were made on opposite sides of the cube and wires were contacted to make 2-point resistivity measurements. The sample was placed in an Infrared Laboratories LHe cryostat for cooling down to 4.2 K. By pumping on the LHe bath in the cryostat the temperature of the sample can be lowered to approximately 1.3 K. For further discussion of the effects of pumping on cryogenic fluids, see Appendix A.

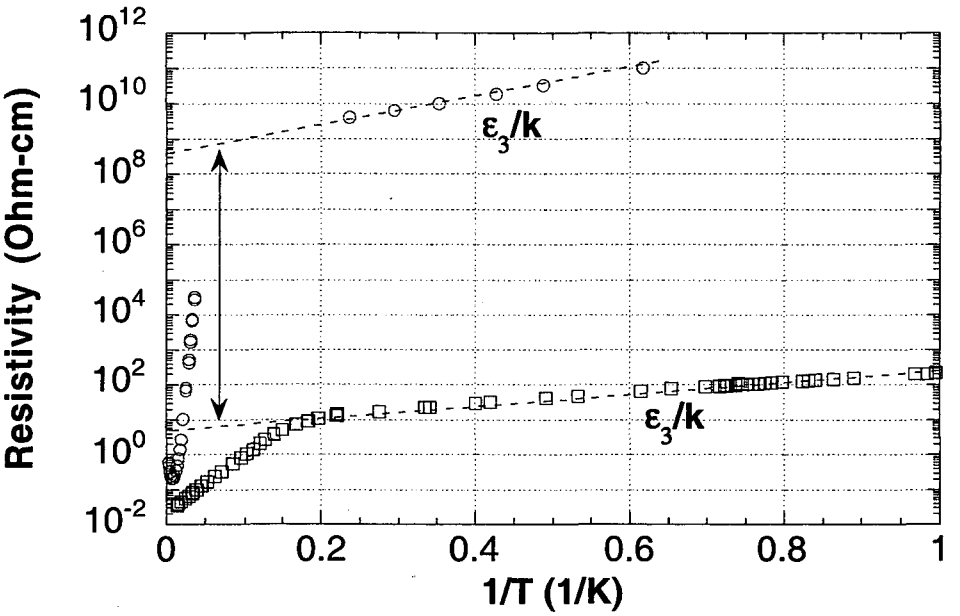

Figure 4.4 Resistivity data for Ge:Cu:Sb sample #831-17 for unstressed (circles) and stressed (squares) samples.

The results of the low temperature resistivity measurements are presented in Figure 4.4. For the unstressed measurement, a tremendous increase in the resistivity can be seen as the temperature decreases. This increase is due to the freeze-out of carriers from the valence band to the isolated Cu atoms with an activation energy of 43 meV. At lower temperatures, the slope of the resistivity decreases. This is due to the onset of hopping conduction. As the concentration of carriers in the band decreases and the corresponding resistivity increases, hopping conductivity between isolated impurity states becomes the dominant conduction mechanism in the material. The slope of the low temperature resistivity of the unstressed Ge:Cu sample corresponds to that of resistivity due to hopping conductivity.

The sample was then stressed above the 4 kbar threshold for the ground state transformation according to the procedure outlined in Section 3.2. Hall effect and resistivity measurements were taken of the stressed sample. The resistivity data is plotted as squares in Figure 4.4. The resistivity is reduced from that of the unstressed sample by

over 8 orders of magnitude. This is a result of the transformation from the 1s state to the 2s state. As described in Equation 1.7, the hopping probability yields a resistivity that varies as the inverse square of the probability density that is dependent on ψ^2. As the extent of ψ increases from 1s to 2s this results in the tremendous decrease in the resistivity seen in Figure 4.4.

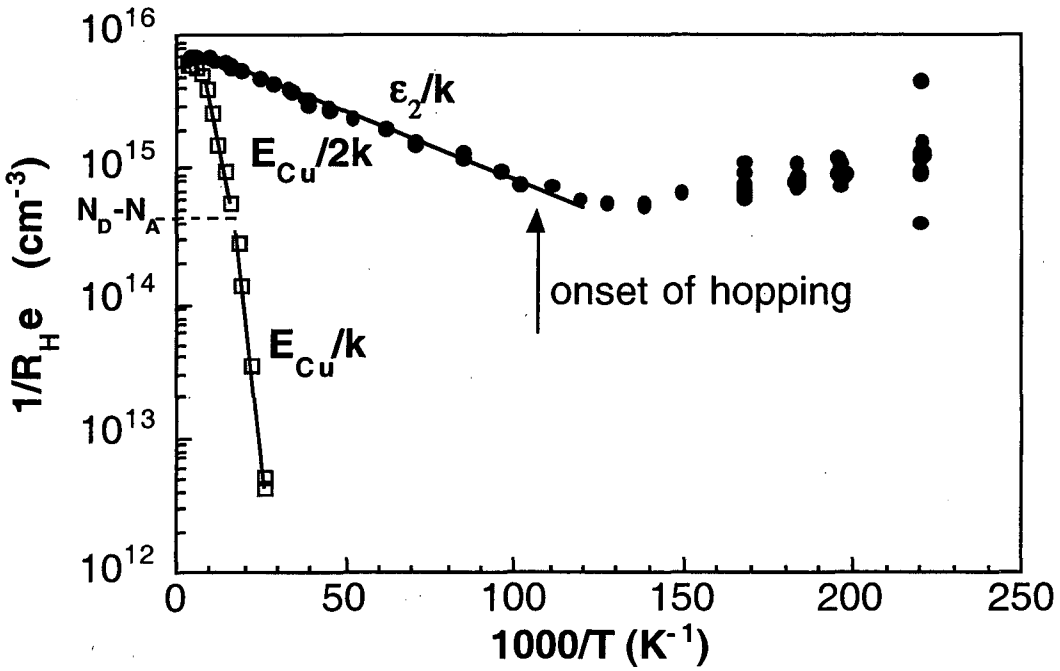

Figure 4.5 Hall effect data for Ge:Cu:Sb sample #831-17; stressed (circles) and unstressed (squares).

The Hall effect data for the stressed and unstressed samples are presented in Figure 4.5. The Hall effect data is plotted as $1/R_H e$, where R_H is the Hall coefficient. The y-axis corresponds to the free hole concentration down to 10 K. Below this temperature, hopping conduction dominates and the y-axis no longer corresponds to the free hole concentration.

The slope of the free carrier freeze-out has changed from a value of 43 meV of the first ionization energy of Cu in Ge in the unstressed sample, to a value of 2.6 meV for the

stressed sample. This 2.6 meV corresponds to the Hubbard gap energy for a Cu concentration of 6×10^{15} cm^{-3}. At temperatures above 10 K, freeze-out of carriers from the upper Hubbard band to the lower Hubbard band gives rise to the shallow slope and the conduction of free carriers within the lower Hubbard band that is responsible for the reduced resistivity seen in Figure 4.4.

The Hall-effect data-points below 10 K show much scatter, no longer continuing the slope of Hubbard gap freeze-out. Such scattering indicates hopping conduction. The phenomenon of the Hall Effect only arises for free carriers within a band, whether it is the valence or conduction band or an impurity band. At this low temperature, the carriers have been frozen out into the much more localized lower Hubbard band. The only means of conduction through the lower Hubbard band at low temperatures is hopping between localized impurity states. This is only possible when there are empty states in the lower Hubbard band. This sample was intentionally doped with Sb to partially compensate the Cu and create empty states in the lower Hubbard band to allow hopping transport. Evidence of hopping transport through the states of the lower Hubbard band is seen in both Figures 4.4 and 4.5.

In the resistivity data of Figure 4.4, the low temperature data ($4 K > T > 0.3 K$) were taken by placing the sample in an Infrared Laboratories LHe cryostat equipped with a L^3He closed cycle refrigerator, which is capable of achieving a temperature as low as 300 mK. A more detailed description of the cryogenics is given in Appendix A. These data show a transition from the Hubbard gap freeze-out induced resistivity activation energy of 2.6 meV to a much more reduced slope (0.25 meV) similar to that of the unstressed case. In the unstressed case the reduced slope is clearly due to the onset of hopping conduction. Based on the Hall effect data of Figure 4.3, it is also believed that the low temperature stressed resistivity is also due to hopping conduction.

The presence of hopping conduction in the lower Hubbard band was verified by comparison to the two primary hopping mechanisms, Variable-Range Hopping (VRH) and Nearest Neighbor Hopping (NNH). The resistivity observed in the lower Hubbard band was determined to be a combination of the resistivity arising from the two mechanisms [36]:

$$\rho_{hop} = \left(\frac{1}{\rho_{NNH}} + \frac{1}{\rho_{VRH}} \right)^{-1} \tag{4.2}$$

The conduction in the lower Hubbard band under partially compensated conditions has been shown to be due to hopping conduction. Hopping conduction is evidenced by the increase in the hopping probability causing an 8 order of magnitude reduction in the resistivity, as well as fitting the data in Figure 4.4 to Equation 4.2, a combination of two hopping mechanisms. The Hall effect data presented in Figure 4.5 also gives evidence of hopping conduction below 10 K.

5 Uniaxially Stressed Ge Doped with Cu and Shallow Acceptors

5.1 Introduction

In order to observe conduction in the upper Hubbard band isolated from the other conduction mechanisms, it must be measured at low temperatures when the other mechanisms are no longer prevalent. In Section 4, conduction in the lower Hubbard band was investigated by doping the Ge:Cu system with shallow donors to create empty states at low temperatures to allow for hopping conduction. To observe upper Hubbard band conduction, carriers must be present in the upper Hubbard band after the holes bound to the Cu have frozen out into the lower Hubbard band. The conduction of these excess carriers would then be observable in the upper Hubbard band without being clouded by the Hubbard gap freeze-out of the acceptors from the Cu impurities.

Following a similar mode to that of Section 4, the Ge samples for these experiments were doped with Cu and shallow acceptors to generate the excess carriers. Figure 5.1 is a schematic Ge energy band diagram showing the presence of excess shallow acceptors and an uncompensated Cu level. The holes from these shallow acceptors should drop down to the Cu states since the Cu states are at a lower energy with respect to holes bound to shallow acceptors. At low temperatures, the lower Hubbard band should be full of the holes from the Cu impurity, leaving the holes from the shallow acceptor to sit in the lowest available level, the upper Hubbard band. A model of the density of states for Ge doped with Cu and shallow acceptors is presented as a schematic in Figure 5.2. The proposed location of the holes from the shallow acceptors at low temperatures can be seen in the diagram.

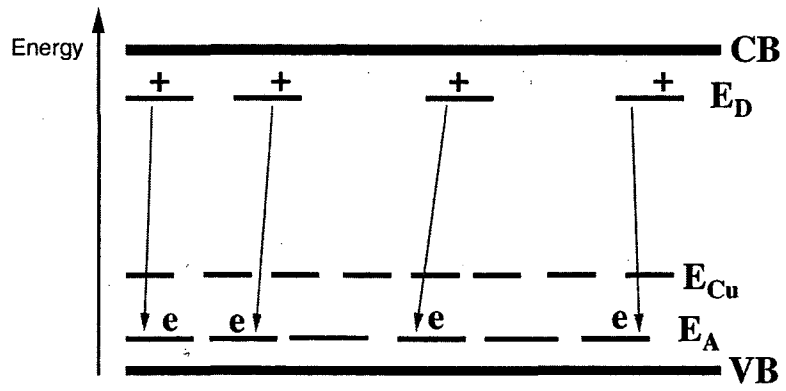

Figure 5.1 Energy band diagram for Ge doped with Cu and shallow acceptors, showing the compensation of shallow acceptors by residual donors.

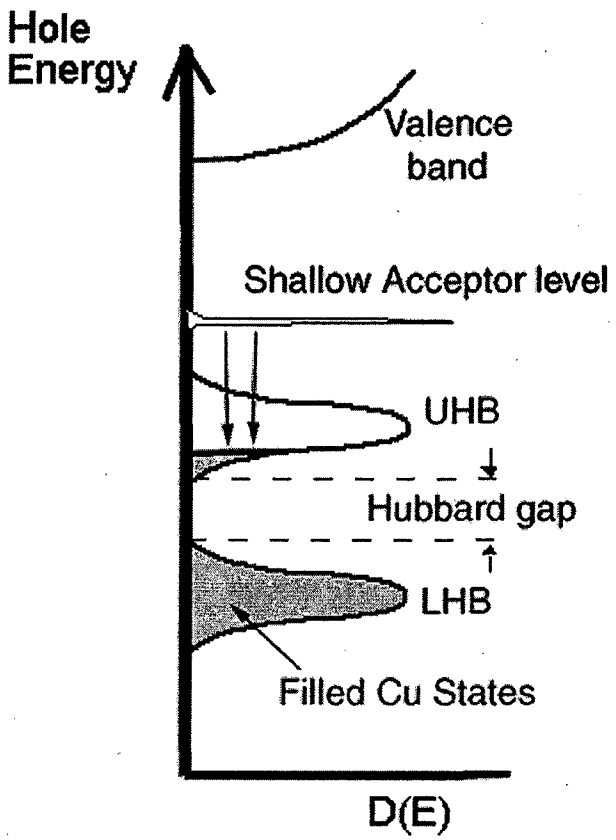

Figure 5.2 Schematic density of states diagram for Ge doped with Cu and shallow acceptors. At low temperatures, holes from the shallow acceptors should occupy the upper Hubbard band.

5.2 Experimental Approach and Results

The samples used to investigate transport in the upper Hubbard band were created from germanium crystals doped during growth with Ga, which acts as a shallow acceptor in Ge. The crystals were then Cu-diffused and processed as described in Section 3.1.

Low temperature resistance measurements were taken on samples with a variety of Cu and Ga concentrations in order to study the conduction mechanisms of the upper Hubbard band.

The free carrier concentration of a sample is presented in Figure 5.3, for both the stressed (circles) and unstressed (squares) cases as measured by Hall effect. The unstressed curve shows the characteristic 43 meV activation energy of unstressed Cu in Ge as well as the saturation level of the shallow acceptor Ga at 4×10^{12} cm^{-3}. The stressed curve has a much shallower slope of 1.6 meV indicative of Hubbard gap freeze-out of a sample with 8×10^{15} cm^{-3} Cu concentration (see Figure 2.4). This freeze-out extends to the lowest temperature capable of the Hall effect apparatus, therefore only resistivity measurements were performed at lower temperatures. The resistivity data is presented in Figure 5.4.

The resistivity measurements indicate two regions with different activation energies. The first, higher temperature region, has an activation energy for the resistivity of 2.6 meV. The second slope occurs at $T < 4$ K, and has an activation energy of 1.2 meV. Taking into account that the resistivity is the product of concentration and mobility, and due to the fact that the resistivity and concentration activation energies are not identical, there must be a contribution from the mobility activation energy of 1 meV.

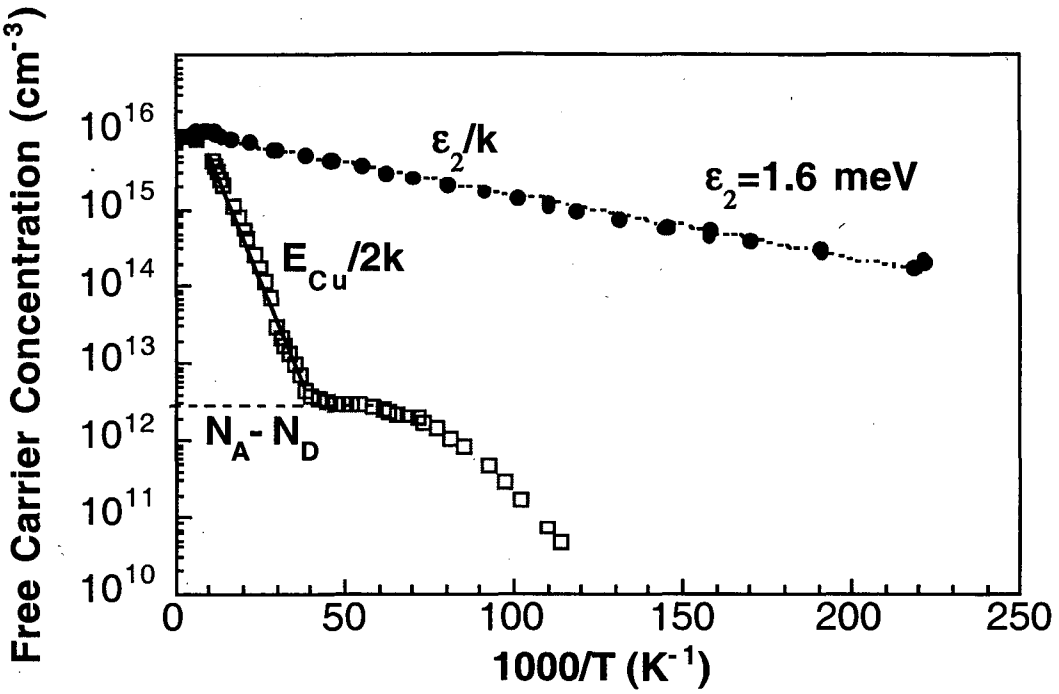

Figure 5.3 Free carrier concentration versus 1000/T for Ge doped with Cu and Ga as determined by Hall effect. Stressed (circles), unstressed (squares).

The mobility data taken from the Hall effect measurement for both the stressed and unstressed samples are presented in Figure 5.5. The unstressed sample shows the expected mobility behavior when plotted versus 1/T. However, the stressed sample shows an activation energy of the mobility of 1 meV, as expected from the resistivity and Hall effect data. This evidence of an activated mobility in the upper Hubbard band also helps to explain the second slope region of Figure 5.4. As more carriers freeze out onto the lower Hubbard band with decreasing temperature, the contribution of the carrier activation energy decreases and the mobility activation energy dominates the resistivity. Therefore, at low temperatures, only the mobility activation energy is present, the carrier activation energy disappears, as evidenced by the resistivity activation energy dropping from 2.6 meV to 1.2 meV.

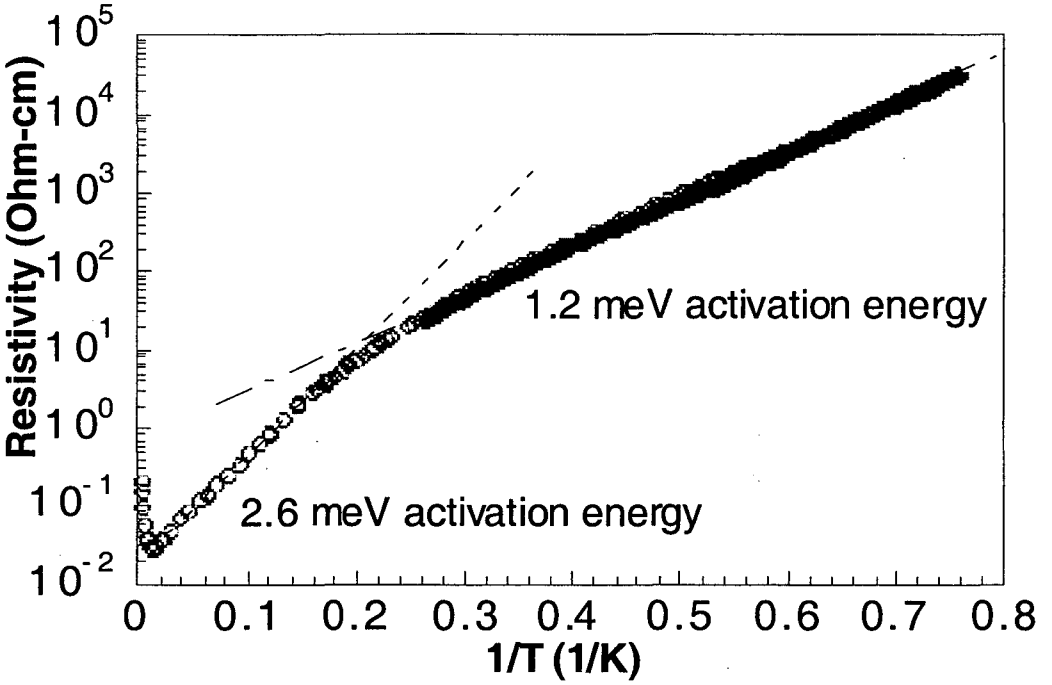

Figure 5.4 Resistivity versus 1/T for Ge doped with Cu and Ga under stress, showing two distinct activation energies.

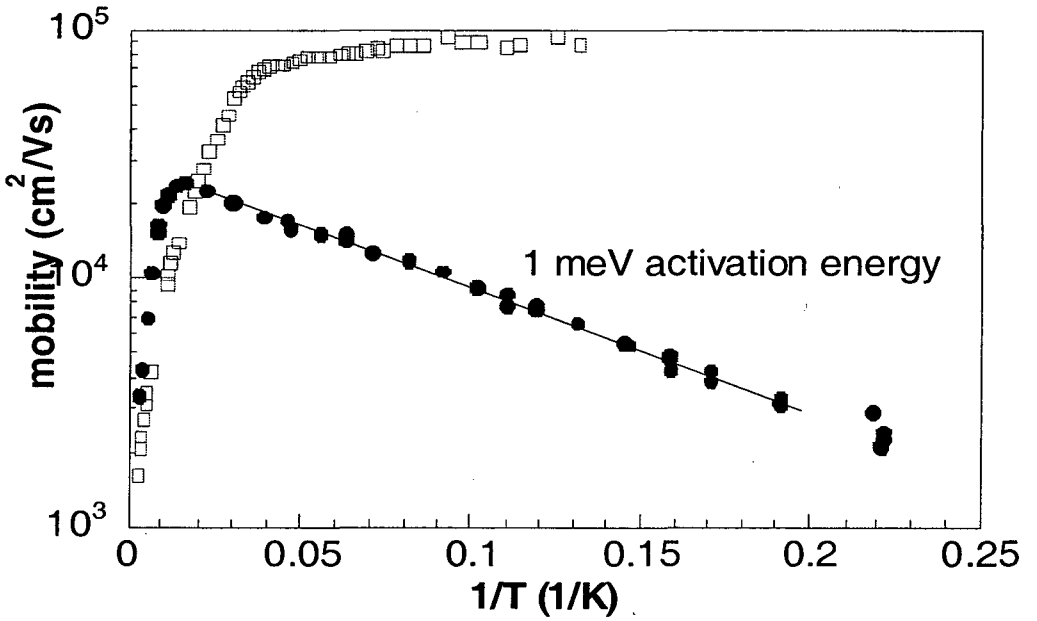

Figure 5.5 Mobility versus 1/T as measured via Hall effect for a Ge sample doped with Cu and Ga. Stressed (circles), unstressed (squares).

Low temperature resistivity measurements were performed on other Cu and shallow acceptor-doped Ge samples under stress, in attempts to observe the same two-slope resistivity seen in Figure 5.4. The results of those measurements are presented together in Figure 5.6. A list of the samples tested is presented in Table 5.1.

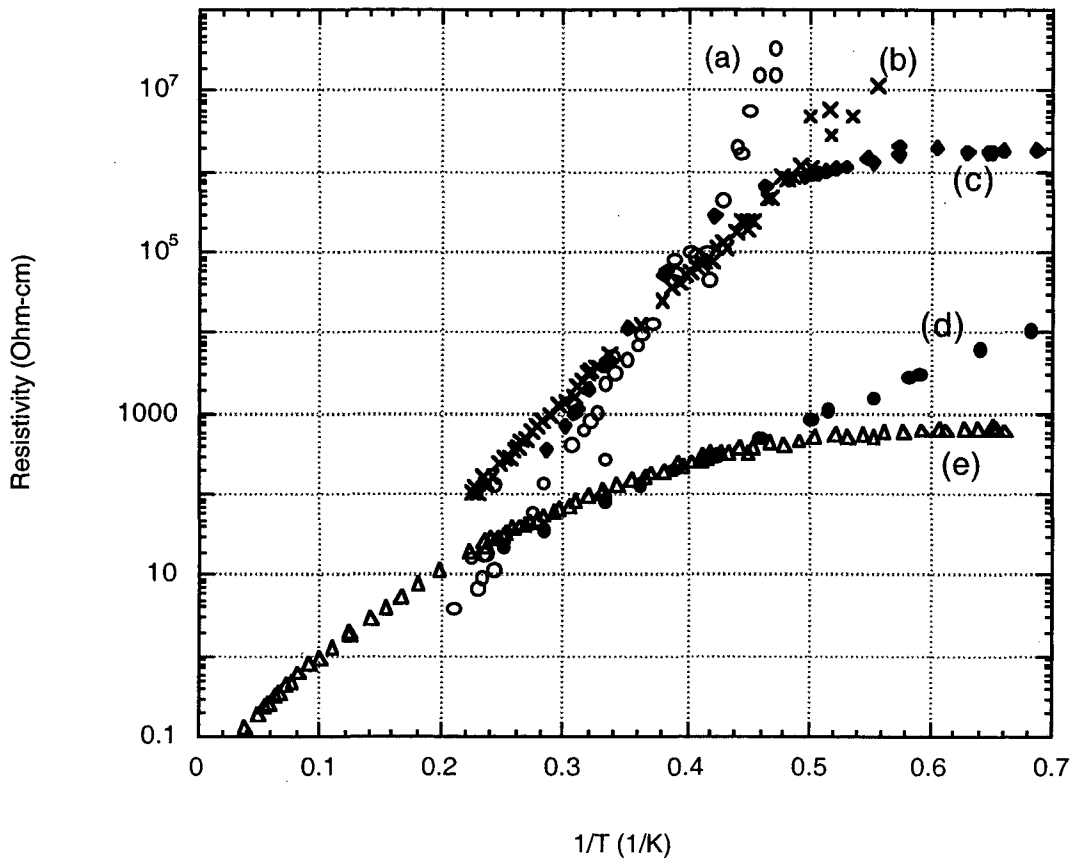

Figure 5.6 Plot of resistivity versus 1/T for samples ranging in Cu concentration from 1.6×10^{14} cm^{-3} to 8×10^{15} cm^{-3}. All samples show the expected Hubbard gap freeze-out in the higher temperature range. The labels correspond to the samples listed in Table 5.1.

From Figure 5.6, it is evident that not all samples display a behavior similar to that of Figure 5.4. They all demonstrate the appropriate Hubbard gap activation energy for the corresponding concentration at $T > 4$ K. Where they differ is in the low temperature regime, $T < 4$ K. Previous work has shown that for samples with [Cu] $\leq 3 \times 10^{15}$ cm^{-3},

the dependence of mobility on temperature is much less than for samples with [Cu] > 3×10^{15} cm^{-3} in the low temperature regime [37]. Figure 5.7 displays the mobility versus temperature for three samples with varying Cu concentrations. Only in the sample with [Cu] > 3×10^{15} cm^{-3} is a highly temperature dependent mobility evident.

Table 5.1 List of samples used for low temperature resistivity measurements under 4 kbar stress. Showing Cu concentration and shallow acceptor concentration.

Sample Label	Cu Concentration (cm^{-3})	Shallow Acceptor Concentration (cm^{-3})
a	1.6×10^{14}	10^{12}
b	2×10^{15}	1×10^{14}
c	3×10^{14}	10^{10}
d	8×10^{15}	4×10^{12}
e	6×10^{15}	1×10^{14}

In this context, the resistivity data presented in 5.6 can be evaluated more clearly. Sample **a**, with a [Cu] of 1.6×10^{14} cm^{-3}, would be expected to show a temperature insensitive resistivity at low temperatures once the mobility becomes the dominant factor in the resistivity. The fact that this is not seen can be attributed to the low concentration and subsequently large Hubbard gap energy of the sample, leading to a transition to the mobility dominated regime at a lower temperature and higher resistivity than were measured for this experiment.

Similar to sample **a**, the data from sample **b** displays a constant slope corresponding to the Hubbard gap energy down to the lowest temperatures measured.

However, unlike sample **a**, sample **b** has a [Cu] of 2×10^{15} cm^{-3} which should lead to the observation of a temperature insensitive, mobility dominated regime at higher temperatures, well within the range measured. The lack of such a region for sample **b** in Figure 5.6, may be attributed to the large shallow acceptor concentration, 1×10^{14} cm^{-3}. The shallow acceptor concentration for samples **b** and **e** is nearly 2 orders of magnitude greater than the other samples tested. The increased ionized impurity scattering may have resulted in these samples deviating from the trend in mobility displayed in Figure 5.7.

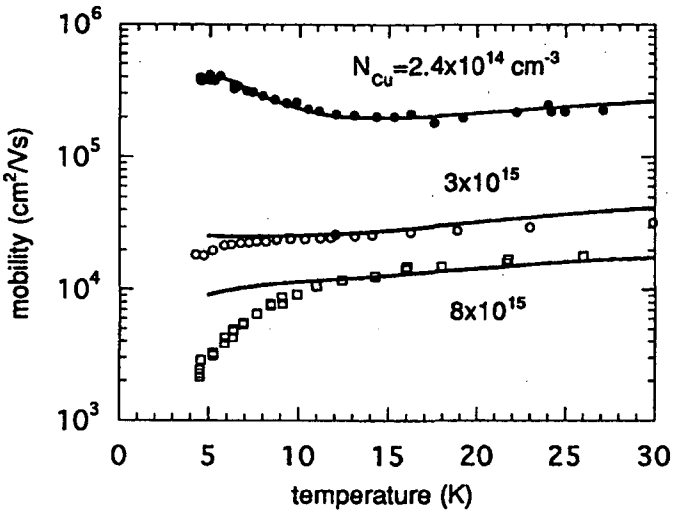

Figure 5.7 Mobility versus temperature data for samples with varying Cu concentrations. Lines are the calculated mobility taking into account neutral and ionized impurity scattering [37].

The resistivity data presented for sample **c** follows the expected dependence on temperature for a sample with a [Cu] of 3×10^{14} cm^{-3}. It has a Hubbard gap energy dependent slope at higher temperatures and then transitions to a temperature insensitive resistivity corresponding to the mobility dominated regime for a sample with a [Cu] $< 3 \times 10^{15}$ cm^{-3}.

Sample **d** is the sample whose resistivity data is also presented in Figure 5.4, and whose temperature dependence was described earlier. The data for this sample certainly fits well within the framework for the temperature dependence of the resistivity of uniaxially stressed Cu-doped Ge presented here. It has a Hubbard gap dependent resistivity at higher temperatures and an activated mobility dependent resistivity at lower temperatures.

Sample **e** is identical to sample **b** in its high shallow acceptor concentration, 1×10^{14} cm^{-3}. However, a difference in the resistivity data due to the higher [Cu] of sample **e** is evident from Figure 5.6. Sample **e** displays a temperature dependent, activated mobility similar to that seen in sample **d** resulting from having a [Cu] $> 3 \times 10^{15}$ cm^{-3}. At the lowest temperatures measured, a third region is seen in the resistivity of sample **e**. A temperature independent resistivity is seen at temperatures below 2 Kelvin. This third region, not seen in other samples, can be attributed to the high shallow acceptor concentration. Sample **e** is very close to sample **d** in its [Cu] and both samples display similar resistivity dependencies in Figure 5.6 above 2 K. Where the two samples differ is in their shallow acceptor concentration. The high shallow acceptor concentration in sample **e** may lead to a larger number of free carriers in the upper Hubbard band. Assuming a similar amount of localization in each sample, which is reasonable considering the similar Cu concentrations, sample **e** would have more delocalized carriers which may result in the temperature independent resistivity seen in Figure 5.6.

A wide range of transport behavior can be seen in the results presented here, demonstrating that the rich potential of this system for studying transport phenomena in semiconductors can not be understood with a single set of experiments. While further experiments are necessary to develop a clearer picture of transport phenomena in uniaxially

stressed Ge:Cu, I have attempted to provide an explanation of the data that is consistent with the current understanding of this system.

6 Magnetic Field Effects on Uniaxially Stressed Ge:Cu

6.1 Introduction

The effects of a magnetic field on impurity states in semiconductors have been studied extensively [38], and the behavior of these states under a magnetic field is well understood. As discussed in Section 2.4, previous work [31,32,33,34] has shown it to be a useful tool in investigating impurity conduction and Metal-Insulator Transitions. The effects of stress and high magnetic field on p-type germanium were investigated by Chroboczek, et al. [39,40]. These studies yielded very interesting information on the behavior of impurities under stress and a magnetic field. These results were used to guide the study of a magnetic field applied to the uniaxially stressed Ge:Cu Hubbard band system in an attempt to reveal more information about the extent of the Cu wavefunctions that form the impurity band.

The application of a magnetic field to a semiconductor has the effect of reducing the dimensions of an impurity wavefunction both parallel and perpendicular to the direction of applied field. The reduction is much greater perpendicular to the field, causing a spherical wavefunction, like the 1s or 2s, to become more cigar-shaped, with the long axis in the direction of applied field.

To describe the effect of the magnetic field on the impurity wavefunction, in the high field limit, Shklovskii defines:[38]

$$a_H = \frac{\hbar}{\sqrt{2mE_H}} \tag{6.1}$$

$$\lambda = \left[\frac{c\hbar}{eH}\right]^{1/2} \tag{6.2}$$

Where a_H is the characteristic length of the wavefunction and is dependent on E_H, the H-field dependent binding energy, m, the effective mass of the carrier, and $\hbar$. The magnetic length is defined by λ, which is dependent on the magnitude of the magnetic field, H. Shklovskii uses these two parameters to determine the surface defining the extent of the wavefunction:

$$\xi = \frac{2|z|}{a_H} + \frac{x^2 + y^2}{2\lambda^2} \tag{6.3}$$

The radii of this surface parallel and perpendicular to the direction of applied field are then given by:

$$\text{parallel}: \quad h = \frac{a_H}{2}\xi \tag{6.4}$$

$$\text{perpendicular}: \quad b = \lambda\sqrt{2\xi} \tag{6.5}$$

By comparing Equations 6.4 and 6.5, it becomes clear that the extent of the wavefunction is reduced to a much greater degree perpendicular to the direction of the applied field.

The magnetic field-dependent resistance perpendicular to the applied field, or perpendicular magnetoresistance, can be defined in the low field limit by the following equation from Mikoshiba [41]:

$$\rho(H) = \rho(0)\exp\left\{t\frac{aH^2e^2}{Nc^2\hbar^2}\right\} \tag{6.6}$$

The magnetoresistance depends exponentially on the square of the magnetic field. The extent of the wavefunction is represented by a in Equation 6.6, while N is the impurity concentration, and t is a fitting parameter.

This magnetoresistance equation (Equation 6.6) describes hopping between isolated impurity states under the influence of a magnetic field. However, hopping conductivity within an impurity band under an applied magnetic field was observed earlier by Sladek in

his studies of InSb [42], leading to the expectation of similar behavior of the uniaxially stressed Ge:Cu Hubbard band system.

6.2 Experimental Approach and Results

Perpendicular magnetoresistance was measured at high B-fields on a variety of samples to determine the effect of a magnetic field on samples with various doping concentrations. A Hall-effect measurement was also performed on one of the samples at high magnetic field in an attempt to determine the carrier concentration of the Hubbard band as a function of magnetic field.

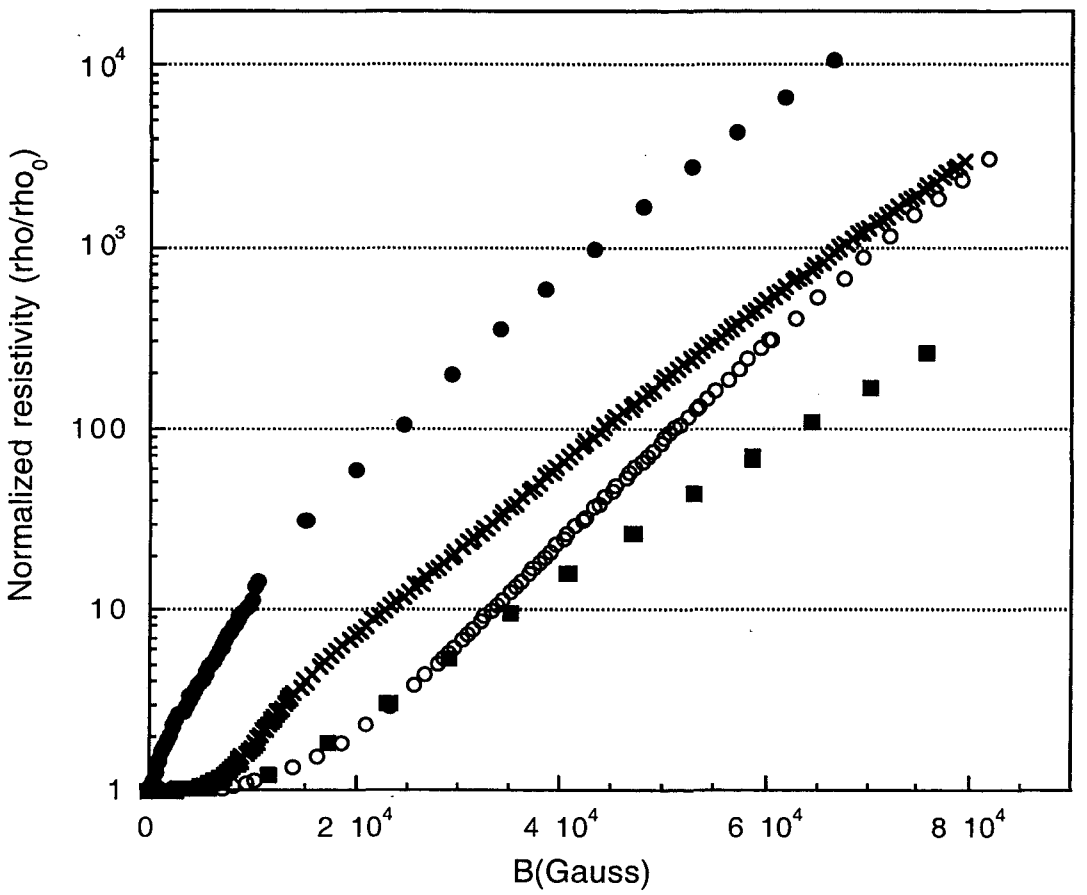

Figure 6.1 Normalized magnetoresistivity data for four Ge:Cu samples with varying Cu concentrations.

The magnetic field was applied by means of a superconducting solenoid magnet with a 1" diameter hole along its length, from Cryomagnetics, Inc. The magnet is immersed in LHe inside a cryostat in order to maintain it at superconducting temperature. The magnet has a maximum B-field of 9 Tesla. Samples are attached to a long rod that acts as a sample holder and lowers the samples down into the magnet. Since the magnet is immersed in LHe, all measurements were performed at 4.2 K. The cryostat has been modified to enable pumping on the LHe bath, which allows for lower temperature measurements.

Figure 6.1 is a plot of normalized magnetoresistance for samples with 4 different Cu concentrations. The filled circles in Figure 6.1 represent a sample with a Cu concentration of 3×10^{14} cm^{-3} and shallow acceptors of ~10^{10} cm^{-3}, the ×'s represent a sample with [Cu] = 2×10^{15} cm^{-3}, [Ga] = 1×10^{14} cm^{-3}, the open circles are for [Cu] = 6×10^{15} cm^{-3}, and [Ga] = 1×10^{14} cm^{-3}. The filled squares are the data from a sample with 1×10^{16} cm^{-3} copper concentration. From this data an H^2 dependence can be observed at low H-fields, while a much weaker $H^{1/2}$ dependence appears at high fields.

Figure 6.2 shows the portion of Figure 6.1 in the low field limit along with a fit to the data according to Equation 6.6. For the fit, a value of 0.025 was used for the percolation parameter, t. This value was taken from Chroboczek [39], and corresponds to p-type Ge under a compressive stress. This equation, which anticipates an exponentially H^2 dependence fits well for the two highly doped samples at low fields, but does not fit well for the two lowest doped samples. This may be due to the fact that the more lightly doped samples have less impurity overlap, so the reduction of the wavefunction induced by the magnetic field (Equation 6.5) breaks apart the band so easily that this expected dependence is not visible. This is reasonable when the onset of the magnetoresistive

behavior is considered. For the lightly doped sample, onset is almost immediate at even the lowest fields. As the impurity concentration increases, and therefore the impurity wavefunction overlap increases, the onset is moved to higher and higher fields. This is a result of increased overlap since the field must diminish the overlap before the hopping behavior described by Equation 6.6 can be observed.

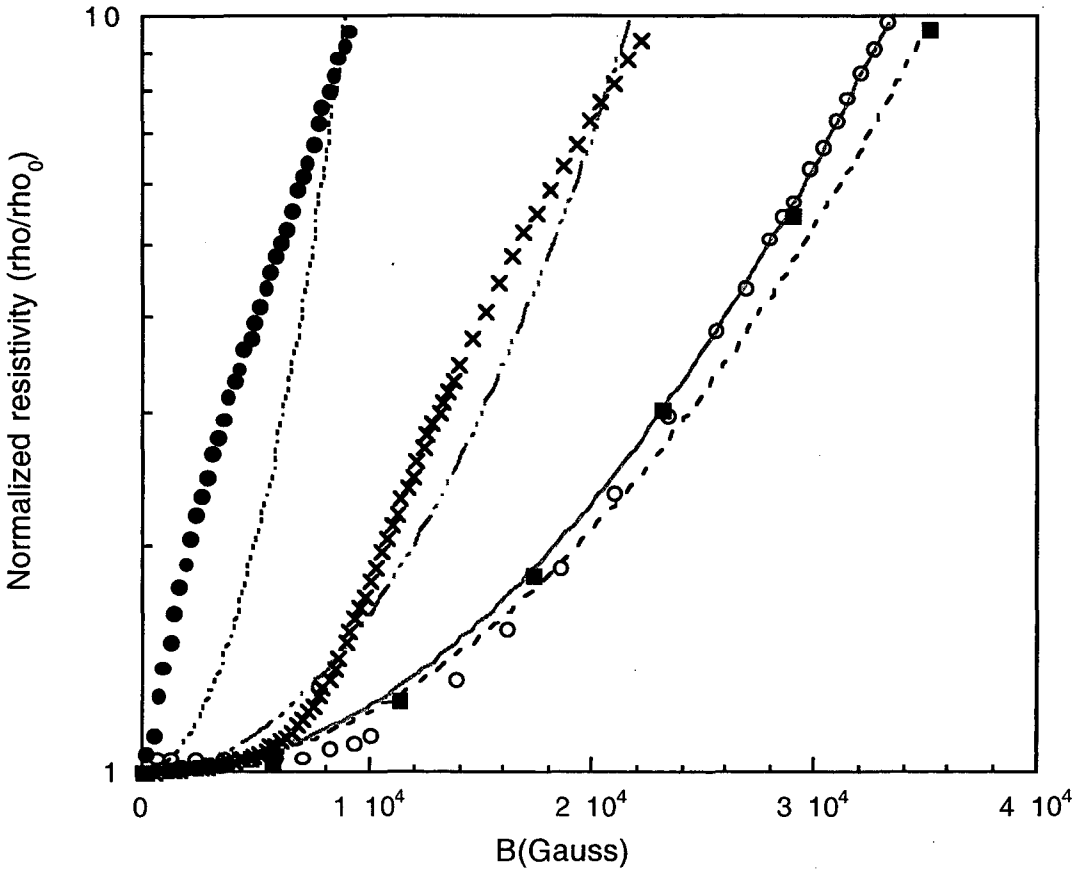

Figure 6.2 Low B-field magnetoresistivity data with a fit to Equation 6.6, using t = 0.025 from Chroboczek [39].

Figure 6.3 shows the measured free carrier concentration versus magnetic field of a 6×10^{15} cm^{-3} [Cu] sample under stress as measured via Hall effect in the superconducting magnet. The measurement was performed on the same system described in Appendix B, modified to allow measurement with the superconducting magnet. The free carriers that are

being measured are in the upper Hubbard band at the measurement temperature. These results show the expected decrease in free carrier concentration of the upper Hubbard band with increasing magnetic field. As the band is disintegrated by the magnetic-field induced reduction of the wavefunction size, fewer impurity states (and their corresponding carriers), are involved in band conduction, leading to the observed reduction in free carrier concentration.

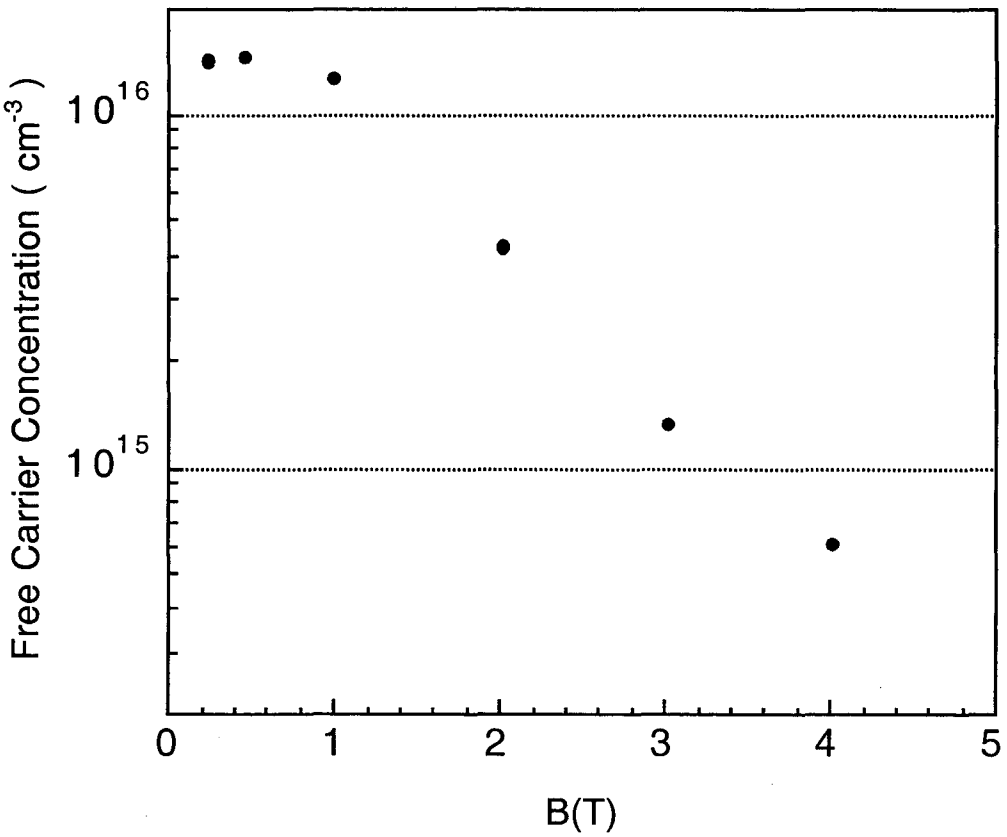

Figure 6.3 Free carrier concentration as a function of magnetic field, measured by Hall effect, for Ge: Cu with a copper concentration of 6×10^{15} cm^{-3}.

7 Conclusions

7.1 Summary

Uniaxially stressed Cu-doped Ge offers many advantages over other material systems when attempting to study impurity conduction and Metal-Insulator Transitions in semiconductors. The relatively deep (E_v + 17 meV) Cu ground state under uniaxial stress, along with the stress-induced ground state transformation, from $(1s)^3$ to $(1s)^2(2s)^1$, lead to the formation of a pair of impurity bands that are well isolated from the valence band and fully separated from each other. This allows the properties of each band to be studied independently.

The lower Hubbard band was studied by the addition of a shallow donor to Cu-doped Ge. This results in the compensation of the states of the lower Hubbard band, causing the formation of empty states in the band. The lower Hubbard band is formed by the neutral ground states of the impurity; so it is normally completely filled, preventing any sort of conduction from occurring. By compensating the material and creating empty states in the lower Hubbard band, conduction should be observed. Hopping conduction, not free carrier-like band conduction, through the lower Hubbard band was observed in a Ge crystal doped with both Sb and Cu. Hopping conduction was observed rather than normal band conduction due to the highly localized nature of the ground state of the impurity. The random distribution of impurities leads to a non-uniform potential throughout the crystal. This may give rise to regions of localized impurity states through which hopping can occur.

In analogy to the successful study of the lower Hubbard band, the upper Hubbard band was studied by means of the addition of shallow acceptors to the Cu-doped Ge crystal. These additional holes should remain in the upper Hubbard band at low

temperatures because it is the lowest energy state available for the holes. These excess holes would then be free to conduct even after all other conduction had ceased at low temperatures. Therefore the hole conduction mechanism in the upper Hubbard band could be studied. From experiments, a change in the resistivity activation energy was seen in the more heavily Cu doped samples, and was attributed to an activated mobility with the upper Hubbard band. The activated mobility was shown to have a concentration as well as a temperature dependence. While the variation of resistivity with temperature can be explained using the data gathered in this work, further investigation into this area is necessary.

A magnetic field was used to reduce the extent of the wavefunction and cause the reduction of the impurity band width. By means of this technique, the band overlap can be varied in much the same way as it was by changing Cu concentration. These experiments yielded magnetoresistance and Hall effect (at high B-field) data that revealed information about the extent of wavefunction and band overlap.

7.2 Future Work

The work reported in this thesis has focused on the transport properties of holes in the Hubbard bands of uniaxially stressed Cu doped Ge at low temperatures. Resistivity measurements (with and without B-field) were the primary means of investigating the transport properties in this work. Any future work must certainly incorporate this technique in order to understand the properties of impurity conduction in the Hubbard bands of Cu-doped Ge. To more effectively use the resistivity experiments, there is a need to measure higher resistances with very low power dissipation at the lowest temperatures, which may require a different experimental approach than the one described here.

Future endeavors should look to other techniques to further the understanding of this system. Hall effect under uniaxial stress proved to be a very useful technique. To be fully employed, it must be combined with the low temperature stressed resistivity data to yield mobility and concentration information in the Hubbard bands. Measurement of the Hall effect at temperatures down to at least 1.3 K would need to be performed to accomplish this task. Another useful area of pursuit would be the continued investigation of the preliminary Hall effect measurements under high magnetic field that were presented in this work.

Most experiments have been performed on samples with Cu concentrations well below the MIT. Studies that incorporate the behavior on the metallic side of the MIT may offer new insights into both conduction within the bands as well as the phenomenon of Metal-Insulator Transitions themselves.

Appendix A: L^3He Refrigerator

This section describes the fundamentals and operation of the L^3He refrigerator used to cool samples down to as low as 300 mK for resistance measurements. More detailed descriptions of cryogens and cryogenic refrigeration techniques can be found in the book by A.C. Rose-Innes [43].

A L^3He refrigerator uses the lower mass isotope of He, ^3He, to obtain temperatures below that achievable with standard LHe. This is due to the fact that the liquid ^3He has a lower normal boiling point (3.2 K) than L^4He (4.2 K). L^3He has a higher vapor pressure than L^4He at all temperatures as well, meaning that one can obtain a lower temperature with L^3He than L^4He at the same pressure, as shown in Figure A.1 [43].

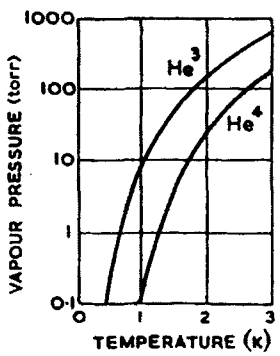

Figure A.1 Vapor pressure versus temperature curves for both He^3 and He^4 [43].

Due to the rarity of ^3He, it is expensive and a closed cycle refrigerator had to be used. The refrigerator consists of a sealed charcoal sorption pump filled with ^3He gas. The charcoal sorption pump was similar in design to the schematic in Figure A.2, except that the pump in Figure A.2 is not closed cycle. It consists of a can of activated charcoal that contains the ^3He gas. The can of charcoal is attached to a heater resistor to allow for the heating of the charcoal. Below the charcoal pump is a copper tube used as a condenser

and below that is a reservoir to collect the L^3He. This reservoir is attached to the sample stage so that the sample stage will be cooled by the L^3He reservoir.

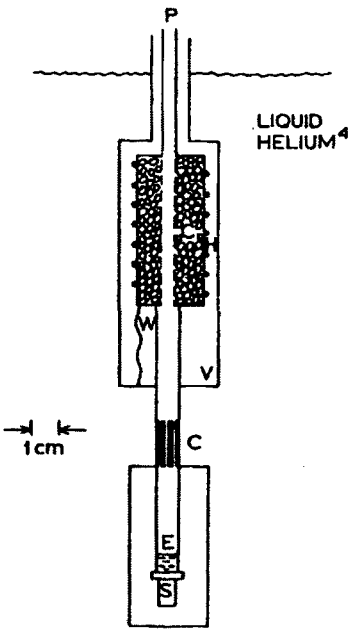

Figure A.2 Schematic of ^3He refrigerator containing a charcoal sorption pump [43].

The fundamental property of the L^3He charcoal sorption pump that makes temperatures of 300 mK attainable is the adsorption of He into the charcoal. Activated charcoal is a porous material with an enormous surface area and when cooled it will adsorb relatively large quantities of He. This is shown in Figure A.3. In this manner, the activated charcoal acts as a pump on the L^3He, lowering its temperature according to Figure A.1. This creates a very simple pump and a closed-cycle refrigerator with no moving parts that can easily be placed in a cryostat.

The L^3He refrigerator was mounted to the cold surface of an Infrared Laboratories, Inc., model HD-3, liquid He cryostat, shown in Figure A.4 [44]. The cryostat was designed such that the LHe storage space could be pumped on in order to lower the temperature of the LHe below 4.2 K.

The operation of the L^3He refrigerator and charcoal sorption pump is as follows: The L^4He is pumped using a mechanical pump to lower the temperature of the L^4He bath to approximately 1.3 K. Since the L^3He refrigerator is mounted on the cold surface of the cryostat, its temperature is reduced to 1.3 K as well. The charcoal sorption pump is then cycled by passing a current (~75 mA) through the heater resistor attached to the charcoal.

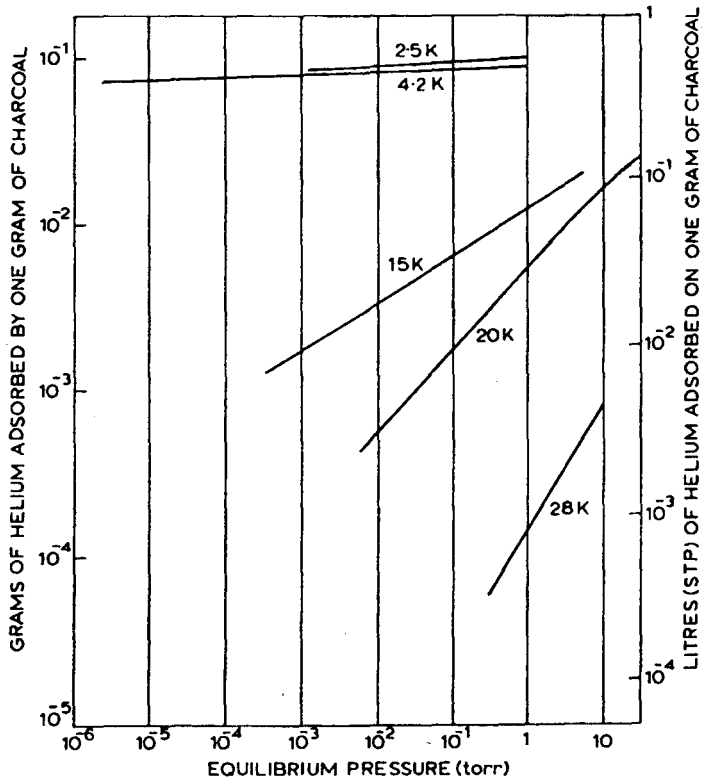

Figure A.3 Helium adsorption on charcoal at varying temperatures. Demonstrating that charcoal can be used as an effective pump on He when cooled [43].

This elevates the temperature of the charcoal, causing desorption of the ^3He gas from the charcoal. The gas then comes in contact with the walls of the refrigerator, which are at 1.3 K. This causes the gas to condense into a liquid and flow into the reservoir where it comes in contact with the sample stage. When the current to the charcoal heater resistor is turned off, the charcoal begins to cool and adsorb any ^3He gas into its pores, effectively pumping on the L^3He bath and lowering the temperature of the bath to around

300 mK. As the system warms up, the L^3He will evaporate entirely and the closed-cycle refrigerator will return to the beginning of its cycle. Depending on the thermal load on the cold stage of the dewar, the hold time at 300 mK can reach up to 4 hours.

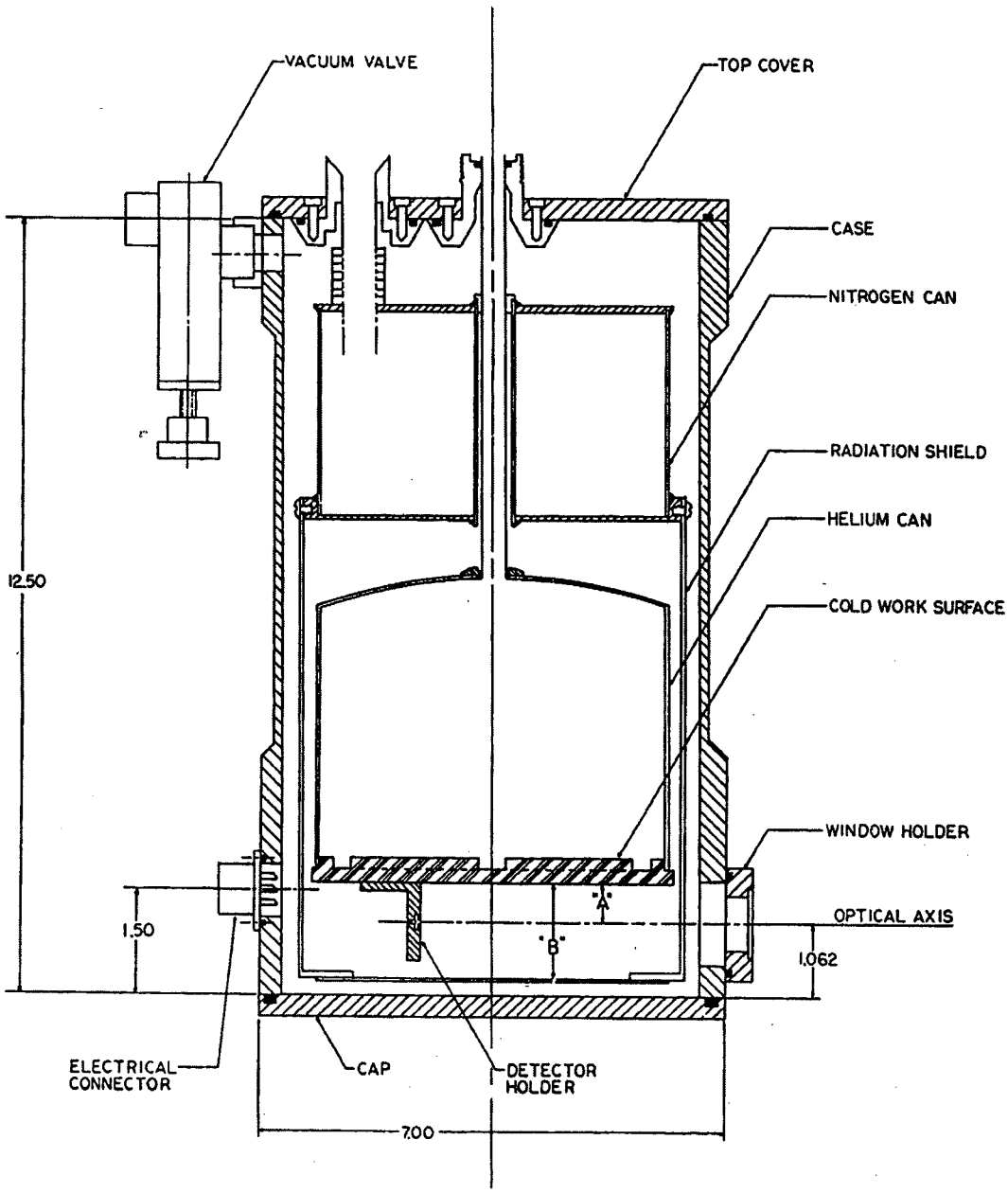

Figure A.4 Schematic of Infrared Laboratories He^4 cryostat; model HD-3. The He^3 refrigerator is mounted to the cold work surface of the cryostat [44].

Appendix B: Hall Effect Measurements

Hall effect measurements were used to determine the majority and minority carrier concentrations, majority carrier activation energy and carrier mobility of the doped germanium samples used in this research. This section will discuss the physical principles behind the Hall effect as well as a description of the Hall effect apparatus used. A more detailed description of the Hall effect and its applications can be found in the article by Beer [45].

B.1 The Hall Effect

The phenomenon known as the Hall effect is named after E.H. Hall. He observed that when a current, I_x, is sent through a piece of metal placed in a magnetic field, B_z, oriented perpendicular to the direction of current, a voltage, V_H, can be detected in the direction mutually perpendicular to both I_x and B_z.[46] This effect is a consequence of the Lorentz force, which is described by:

$$\vec{F_L} = q\left(\vec{v} \times \vec{B}\right) \tag{B.1}$$

where F_L is the Lorentz force, q is the charge of the particle, v is its drift velocity, and B is the magnetic field vector. The drift velocity can be written in terms of the applied current, as $v_x=I_x/(nqtw)$, where I_x is the current in the x-direction, n is the majority carrier concentration, t is the sample thickness and w is the sample width. According to the Lorentz equation, which uses the cross product of the velocity and magnetic field vectors, a particle moving in a magnetic field will feel a force that is mutually perpendicular to both the velocity and magnetic field directions. The effect of this force on the charge carriers is to cause them to be deflected in the direction of the force, F_L. This results in the creation of

an electric field across the crystal, E_H. The electric field imposes a force, F_E, on the charge carriers in opposition to the Lorentz force:

$$F_E = qE_H \tag{B.2}$$

where q is the charge on the carriers. Equations B.1 and B.2, the relationship for the drift velocity, and the relationship $E_H = V_H/w$, (where w is the width of the crystal and V_H is the

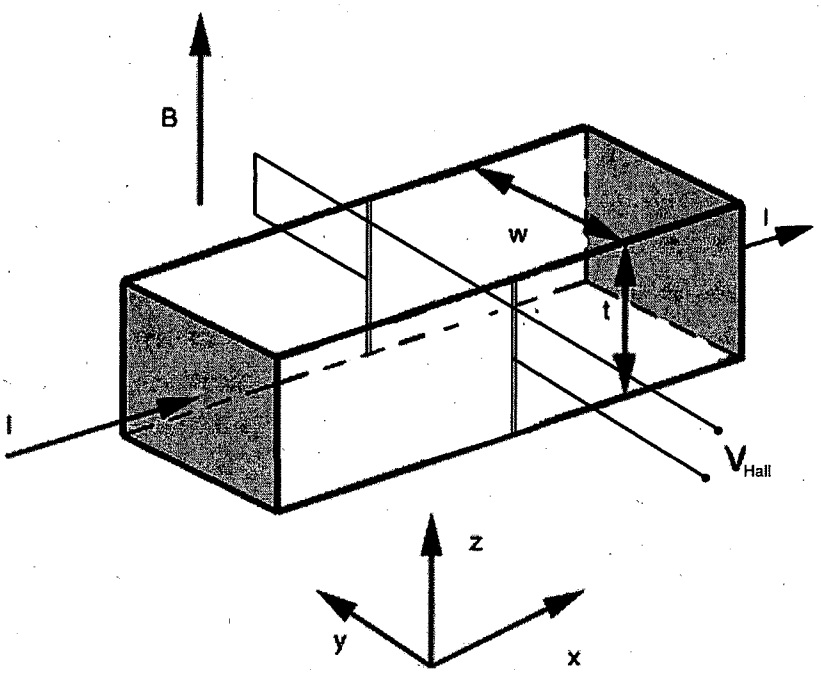

Figure B.1 A schematic of the Hall bar configuration for measurement of the Hall effect. The schematic shows the direction and relative orientation of the current, voltage, and magnetic field.

voltage induced by the electric field), along with the fact that the two forces F_L and F_E must balance within the crystal, gives

$$q\left(\frac{I_x}{nqtw}\right)B_z = q\frac{V_H}{w} \tag{B.3}$$

and

$$\frac{1}{R_H} = \frac{I_x B_z}{tV_H} \tag{B.4}$$

In equation B.4, R_H is the Hall coefficient defined as 1/qn. The voltage, V_H, is the Hall voltage. Equation B.4 is very useful because the quantities I_x, B_z, t, and V_H, can all be measured. This allows the determination of the free carrier concentration, n, from R_H. The Hall coefficient itself reveals some information about the sample. If R_H is positive, the majority carriers are holes and if R_H is negative, the carriers are electrons.

By combining the measurement of the Hall coefficient with a resistivity measurement, the mobility can be calculated from the resistivity equation $\rho=1/(nq\mu,)$, giving,

$$\mu = \frac{R_H}{\rho} \tag{B.5}$$

where μ is the mobility of the charge carriers.

B.1.1 The van der Pauw Geometry

It is often not possible or not convenient to use a sample for Hall effect with the Hall bar geometry seen in Figure B.1. Many semiconductors are processed in the form of wafers or thin films, making the creation of a Hall bar difficult if not impossible. It was demonstrated by van der Pauw [47], that the Hall effect can be measured in a flat sample of arbitrary shape. He imaged a singly connected sample of constant thickness by a conformal transformation on to an infinite half plane. The boundary of the half plane corresponds to the perimeter of the sample. In order for his transformation to work, the electrical contacts must be located at the circumference of the sample, they must be sufficiently small, the sample must be homogeneous in thickness and the sample surface must be continuous, i.e., it has no holes. van der Pauw proved that if the sample meets the above conditions, the four-point resistance is invariant under conformal transformation.

Therefore, the contacts can be located at arbitrary points and the resistance and Hall effect can still be measured.

van der Pauw expressed the resistivity as [47]:

$$\rho = \frac{\pi\delta}{\ln 2}\frac{R_{12,34} + R_{23,41}}{2} f \tag{B.6}$$

Where δ is the thickness of the sample, $R_{12,34}$ represents the resistance measured by passing a current through contacts 1 and 2 and measuring the voltage through contacts 3 and 4, and f is a parameter to account for the sample geometry. Contacts 1,2,3, and 4, are sequentially located around the perimeter of the sample. A plot showing the factor f as a function of the anisotropy of the resistance is given in Figure B.2.

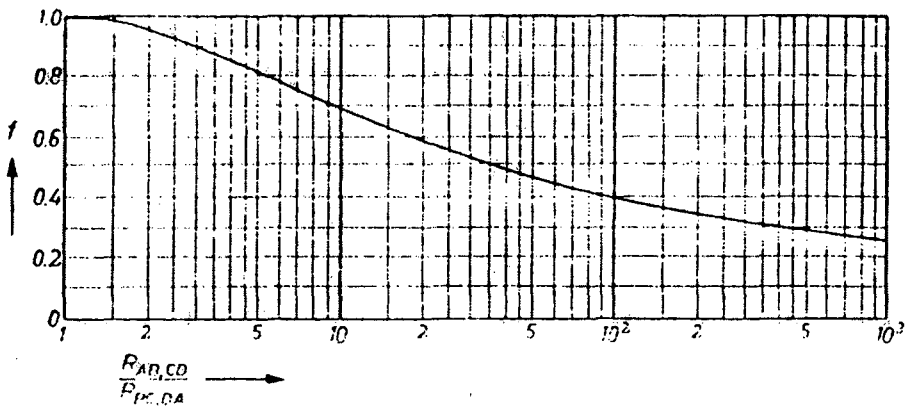

Figure B.2 Plot of the factor f as a function of the sample resistance anisotropy. [47]

From Figure B.2, it can be seen that for samples with an anisotropy ratio as large as a factor of 2, the use of a value of 1 for the f factor is still sufficient.

The Hall coefficient from van der Pauw's calculations is given as:

$$R_H = \frac{\delta \Delta R_{24,13}}{B} \tag{B.7}$$

Where $\Delta R_{24,13}$ is the change in resistance due to the magnetic field, and B is the magnetic field. From these equations the same information can be extracted as from the standard Hall effect geometry described above.

B.2 Experimental Apparatus

The Hall effect apparatus used in the experiments consists of two major parts, the electronics used to control the instruments and the instruments used to vary the experimental parameters. A Keithley Instruments System 110 Hall System was used as the basis of the electronic controls of our Hall effect measurement. The System 110 performs all the current and voltage measurements and current output. A schematic of the System 110 Hall System is presented in Figure B.3.

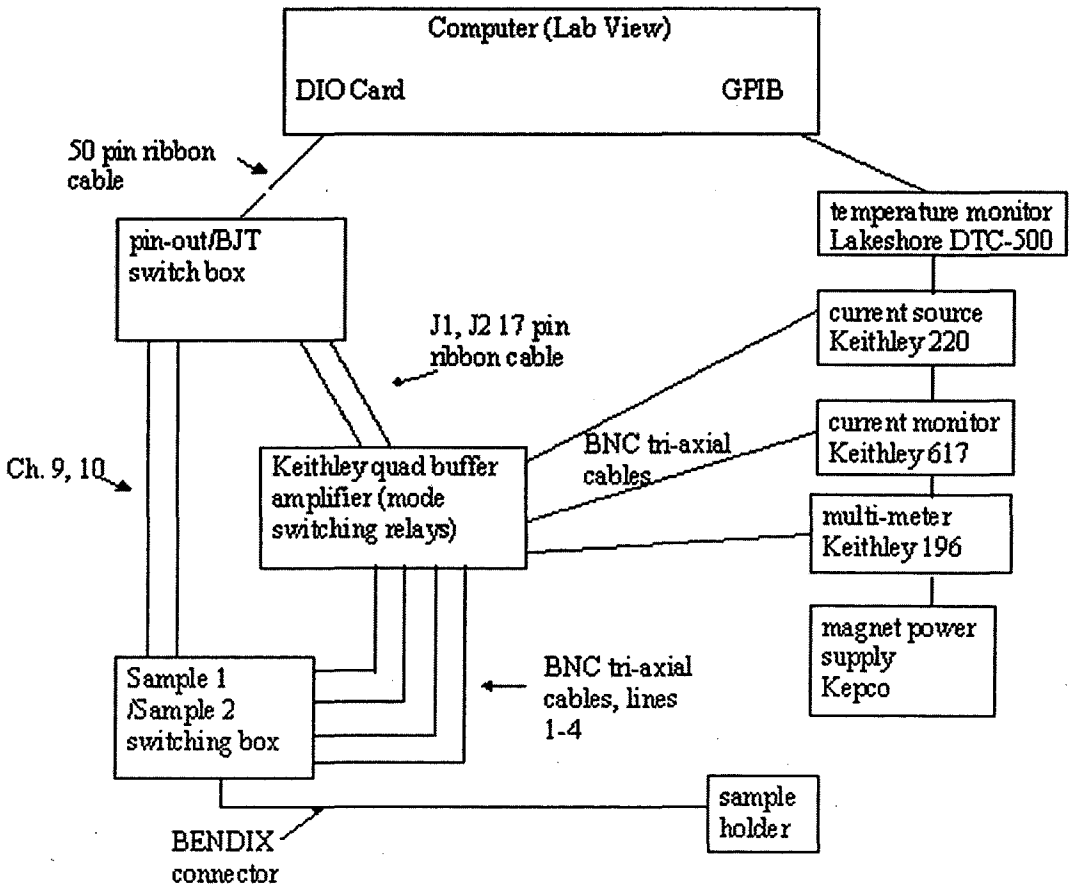

Figure B.3 Layout of the Keithley Instruments, System 110, Hall System, containing the system controller, current source, electrometer, multiprogrammer and buffer amplifiers. [Courtesy of Ben Cardozo]

All instruments in the system are GPIB addressable and are controlled by a GPIB card in the computer. The a digital I/O card sends commands via a ribbon cable to the Buffer Amplifier Relay module, which contains relays that allow for the switching of the orientation of current and voltage contacts, necessary in a van der Pauw Hall-effect measurement. Four isolated triaxial cables are connected between the Buffer Amplifier Relay Module and the sample cryostat. These cables act as the four signal lines for current and voltage measurement. The triax cables along with the Buffer Amplifier Relay Module allow for greater isolation of the signal and therefore a reduction in noise induced on the signal lines. The inner shield of the triax cable is kept at the same potential as the signal line by means of a feedback amplifier. Since there is no difference in potential between the two lines, no charge can be induced on the signal line through microphonics or other mechanical distortion of the triax cable. An induced charge would cause errors in the measurement. The relays in the Buffer Amplifier Relay module are high impedance relays to further isolate each signal and reduce the noise.

A LakeShore CT-310 LHe flow cryostat is used to vary the temperature from 300 K to 4.2 K. A schematic of the cryostat is given in Figure B.4. The transfer line is inserted into a LHe storage dewar. By pressurizing the dewar, LHe flows through the transfer line where it comes in contact with a cold finger that leads down into the evacuated sample space. The sample space is evacuated by a diffusion pump to prevent condensation of air on the sample. After coming in contact with the cold finger, the LHe vapor is vented out through a flowmeter. By controlling the flow rate of LHe and using a Lakeshore model DTC 500-SP Cryogenic Temperature Controller, the temperature can be controlled down to 4.2 K and stabilized at any temperature to allow for a measurement to be taken. Temperature measurements were made using a LakeShore DRC-80 cryogenic thermometer.

The sample end of the cryostat is inserted between the poles of an electromagnet controlled by a Kepco Bipolar Power Supply. For these experiments a 3-kiloGauss magnetic field was used.

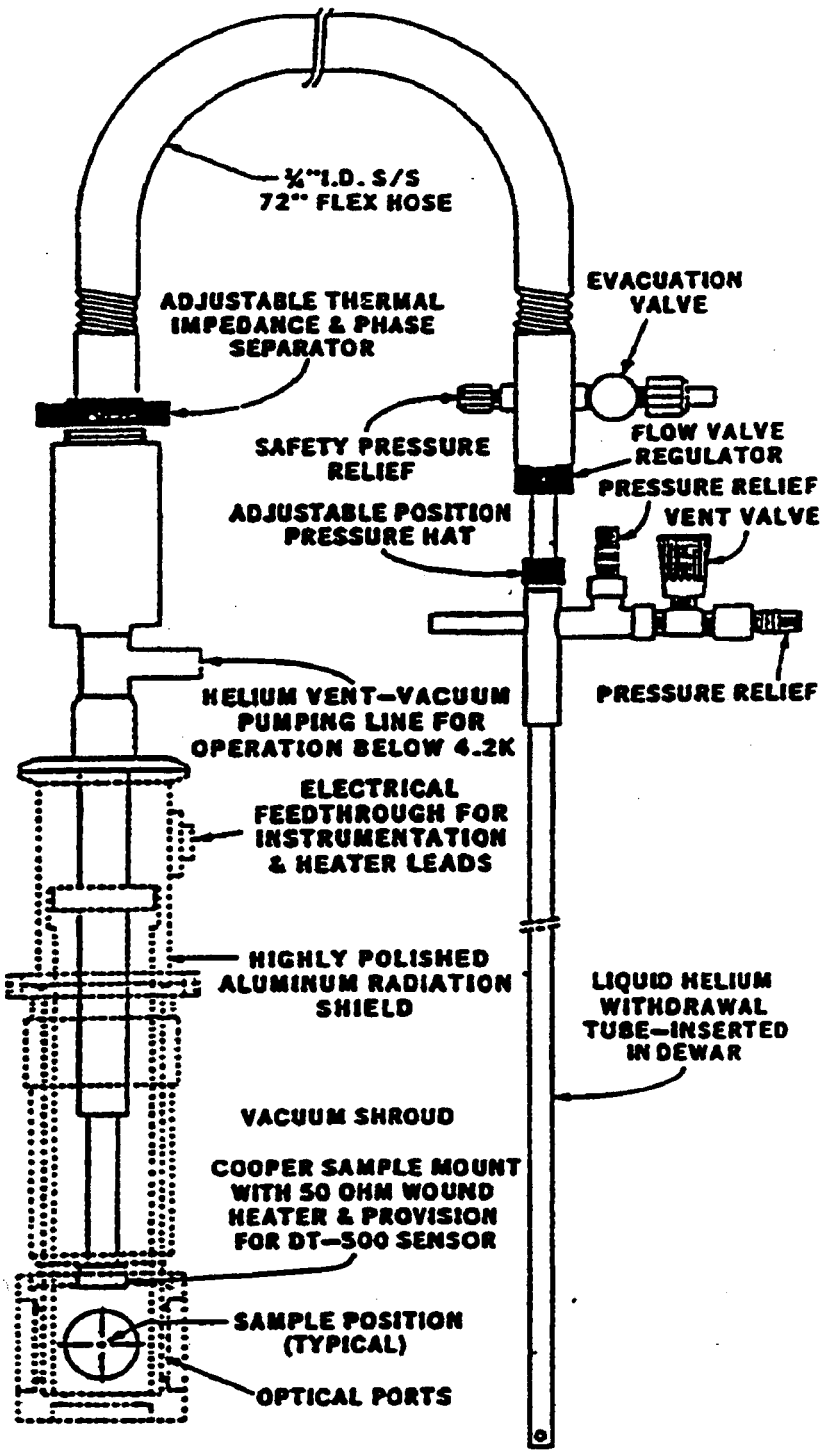

Figure B.4 Schematic of LakeShore CT-310 continuous flow cryostat.

8 References

1. H.A. Bethe, "Theory of the boundary layer of crystal rectifiers", MIT Radiation Laboratory Report 43-12, 1942.

2. C. Kittel and A.H. Mitchell, *Phys. Rev.* **96**, 1488 (1954).

3. J.M. Luttinger and W. Kohn, *Phys. Rev.* **97**, 869 (1955).

4. E.E. Haller, W.L. Hansen, F.S. Goulding, "Physics of ultra-pure germanium", *Advances in Physics*, **30**, No. 1, 1981, p. 93-138

5. B.A. Andreev, G.G. Devyatykh, V.A. Gavva, D.M. Gordeev, A.V. Gusev, G.A. Maksimov, V.G. Pimenov, V.B. Shmagin, and D.A. Timonin, *Semicond. Sci. Technol.* **9**, 1050 (1994).

6. H.H. Woodbury and W.W. Tyler, *Phys. Rev.* **105**, 84 (1957).

7. C.S. Fuller and J.C. Severiens, *Phys. Rev.* **96**, 21 (1954).

8. F.C. Frank and D. Turnbull, *Phys. Rev.* **104**, 617 (1956).

9. N A. Stolwijk, W. Frank, J. Holzl, S.J. Pearton, and E.E. Haller, *J. Appl. Phys.* **57** (12) 5211 (1985).

10. A.S. Barker and A.J. Sievers, *Reviews of Modern Physics* **47**, Suppl. No. 2 (1975).

11. R.N. Hall and J.H. Racette, *J. Appl. Phys.* **35**, 379 (1964).

12. H. Bracht, N.A. Stolwijk, and H. Mehrer, *Phys. Rev. B* **43**, 14465 (1991).

13. A.G. Tweet, *Phys. Rev.* **106**, 221 (1957).

14. A.G. Yakovenko and E.A. Shelonin, *Sov. Phys. Semicond.* **23**, 865 (1989).

15. P. Clauws, G. Huylebroeck, E. Simoen, P. Vermaercke, F. De Smet, and J. Vennik, *Semicond. Sci. Technol.* **4**, 910 (1989).

16. E.H. Salib, P. Fisher, and P.E. Simmonds, *Phys. Rev. B* **32**, 2424 (1985).

17. E.E. Haller, R.E. McMurray, Jr., N.M. Haegel, and L.M. Falicov, *Proc. of the 17th International Conf. on the Phys. of Semiconductors*, 679 (1985).

18. J.R. Chelikowsky and M.L. Cohen, *Phys. Rev. B* **14**, 556 (1976).

19. G.E. Pikus and G.L. Bir, *Soviet Physics – Solid State* **1**, 1502 (1960).

20. R. Buczko, *Nuovo Cimento D* **9**, 669 (1987).

21. O.D. Dubon, J.W. Beeman, L.M. Falicov, H.D. Fuchs, E.E. Haller, and C. Wang, *Phys. Rev. Lett.* **72**, 2231 (1994).

22. N.F. Mott and Z. Zinamon, *Rep. Prog. Phys.* **33**, 881-940 (1970).

23. B.I. Shklovskii, *Sov. Phys. – Semicond.* **6**, 1053 (1973).

24. A. Miller and E. Abrahams, *Phys. Rev.* **120**, 745 (1960).

25. J. Hubbard, *Proc. Roy. Soc.* **A276**, 238 (1963).

26. H. Fritzsche and M. Cuevas, *Phys. Rev.* **119**, 1238 (1960).

27. B.V. Rollin and J.P. Russell, *Proc. Phys. Soc.* **81**, 571 (1963).

28. O.D. Dubon, Ph.D. thesis, University of California, Berkeley (1996).

29. O.D. Dubon, W. Walukiewicz, J.W. Beeman, and E.E. Haller, *Phys. Rev. Lett.* **78**, 3519 (1997).

30. X. Liu, A. Sidorenko, S. Wagner, P. Ziegler, and H.v. Lohneysen, *Phys. Rev. Lett.* **77**, 3395 (1996).

31. V.J. Goldman, M. Shayegan, and H.D. Drew, *Phys. Rev. Lett.* **57**, 1056 (1986).

32. S. Liu, H.D. Drew, A. Illiades, and S. Hadjipanteli, *Phys. Rev. B* **45**, 1155 (1992).

33. W.N. Shafarman, T.G. Castner, J.S. Brooks, K.P. Martin, and M.J. Naughton, *Phys. Rev. Lett.* **56**, 980 (1986).

34. P.F. Hopkins, M.J. Burns, A.J. Rimberg, and R.M. Westervelt, *Phys. Rev. B* **39**, 12 708 (1989).

35. J.–Q. Wang, P.L. Richards, J.W. Beeman, and E.E.Haller, *Applied Optics* **26**, 4767 (1987).

36. O.D. Dubon, H.H. Silvestri, W. Walukiewicz, E.E. Haller, *Solid State Communications* **117**, 537 (2001).

37. W. Walukiewicz, O.D. Dubon, H.H. Silvestri, and E.E. Haller, *Phys. Stat. Sol.* (b) **210**, 253 (1998).

38. B.I. Shklovskii and A.L. Efros, "Electronic Properties of Doped Semiconductors", Springer-Verlag, New York, 1984.

39. J.A. Chroboczek, H . Fritzsche, C.-L. Jiang, M. Pollack, and R.L. Wild, *Phil. Mag. B* **44**, 685 (1981).

40. J.A. Chroboczek, *Phil. Mag. B* **42**, 933 (1980).

41. N. Mikoshiba, *Phys. Rev.* **127**, 1962 (1962).

42. R.J. Sladek, *J. Phys. Chem. Solids* **5**, 157 (1958).

43. A.C. Rose-Innes, Low Temperature Laboratory Techniques, Crane, Russack, & Co., New York, 1973.

44. Owners Manual, Model HD-3, Infrared Laboratories, Inc., Tucson, AZ.

45. A.C. Beer, in *The Hall Effect and its Applications* C.L. Chien, C.R. Westgate, Eds. (Plenum Press, New York, 1980) pp. 299-338.

46. E.H. Hall, *Amer. J. Maths.* **2**, 287 (1879).

47. L.J. van der Pauw, *Philips Res. Rep.* **13**, 1 (1958).

Ernest Orlando Lawrence Berkeley National Laboratory
One Cyclotron Road | Berkeley, California 94720

Prepared for the U.S. Department of Energy under Contract No. DE-AC03-76SF00098